Methods[1]

Expedition 333 Scientists[2]

Chapter contents

[1] Expedition 333 Scientists, 2012. Methods. *In* Henry, P., Kanamatsu, T., Moe, K., and the Expedition 333 Scientists, *Proc. IODP,* 333: Tokyo (Integrated Ocean Drilling Program Management International, Inc.). doi:10.2204/iodp.proc.333.102.2012
[2] **Expedition 333 Scientists' addresses.**

Introduction

This chapter documents the methods used for shipboard scientific analyses, including sample collection, preparation, and preservation for either shipboard or shore-based analysis. This information can be used to understand the means by which we arrived at preliminary conclusions and interpretations. It also provides information for those interested in ancillary analyses, shore-based sampling, or integrative investigations.

This chapter explains coring techniques, core handling, and the numbering of sites, holes, cores, sections, and samples. In most cases, this information mirrors the details described in previous volumes of the *Proceedings of the Integrated Ocean Drilling Program,* particularly Expedition 322. However, because of the relationship between this expedition and the other expeditions that comprise the Nankai Trough Seismogenic Zone Experiment (NanTroSEIZE) and the large number and volume of sample requests, there are significant differences that are explained below.

Site locations

Integrated Ocean Drilling Program (IODP) Expedition 333 site locations were selected based on precruise surveys and the overall goals of NanTroSEIZE. Onboard GPS satellite navigation was used to position the vessel using dynamic positioning, and acoustic beacons deployed on the seafloor provided additional means of acquiring and keeping vessel position during operations. Because the remotely operated vehicle was not deployed in the >3000 m water depth, a precise fix on the location of the borehole was not obtained upon spud-in. The ship's position was used as the borehole position.

Drilling operations

Four coring systems were employed during Expedition 333:

1. Hydraulic piston coring system (HPCS), equivalent to the advanced piston coring (APC) system employed on the R/V *JOIDES Resolution,*
2. Extended punch coring system (EPCS) developed during IODP Expedition 316 by combining pieces from the HPCS, extended shoe coring system (ESCS), and rotary core barrel (RCB) system to extend the range of the HPCS to more consolidated sediments,

doi:10.2204/iodp.proc.333.102.2012

3. ESCS, equivalent to the extended core barrel (XCB) system employed on the *JOIDES Resolution*, and
4. RCB.

The cored interval is measured in meters below seafloor (mbsf) according to the core depth below seafloor, method B (CSF-B), depth scale (see IODP Depth Scale Terminology at **www.iodp.org/program-policies/**). Drilled intervals are initially referred to in drilling depth below rig floor (DRF), which is measured from the kelly bushing on the rig floor to the bottom of the drill pipe, and is later converted to core depth below seafloor (CSF). The height of the rig floor is 28.3 m above the mean sea level. During Expedition 333, all core depths below seafloor were calculated as CSF-B, and reported in this volume as "meters below seafloor" unless otherwise noted (CSF in physical properties uses Method A).

Drilling-induced core deformation

X-ray computed tomography (CT) imagery and direct inspection of split cores often reveal significant evidence for disturbance of recovered materials. For example, during RCB coring deformation results from rotation and "spiraling" of sections of cores, "biscuiting" of small sections of core and injection of either drilling mud or finely ground material produced at the drill bit into spaces between individual biscuits, or brecciation or grinding of material before collection into the core liner/core barrel. Core deformation may also result from depressurization, expansion, and thermal equilibration of the core as it travels up the drill string, during handling on deck, and during core cutting and splitting. Where possible, such core disturbance was noted in core descriptions.

Numbering of sites, holes, cores, sections, and samples

Sites drilled by the D/V *Chikyu* are numbered consecutively from the first site with a prefix "C." A site refers to one or more holes drilled while the ship is positioned within 300 m of the first hole. The first hole drilled at a given site is assigned the site number modified by the suffix "A," the second hole takes the site number and suffix "B," and so forth. These suffixes are assigned regardless of recovery, as long as penetration takes place. Cored intervals are calculated based on an initial 9.5 m length, which is the standard core barrel length for each coring system. In addition, we specified the collection of shorter coring intervals in areas of poor recovery or slow rate of penetration. Expansion of cores in the upper sections (and sucked-in material) and gaps related to unrecovered material result in recovery percentages greater or less than 100%, respectively. Depth intervals are assigned starting from the depth below seafloor at which coring started (IODP coring depth scale calculated using Method B [CSF-B]; see IODP Depth Scales Terminology at **www.iodp.org/program-policies/**). Short cores (incomplete recovery) are all assumed to start from that initial depth by convention. Core expansion is corrected during final processing of core measurements by subtracting void spaces, subtracting exotic material, and accounting for expansion (IODP coring depth scale calculated using Method B [CSF-B]).

A recovered core is typically divided into 1.4 m long sections that are numbered serially from 1 beginning at the top. During Expedition 333, whole-round core samples were removed for interstitial water sampling and assigned their own section number in order to allow for rapid X-ray CT scanning of time-sensitive samples. Material recovered from the core catcher was assigned to a separate section, labeled core catcher (CC), and placed at the bottom of the lowermost section of the recovered core.

A full identification number for a sample consists of the following information: expedition, site, hole, core number, core type, section number, and top to bottom interval in centimeters measured from the top of the section. For example, a sample identification of "333-C0012G-2R-5, 80–85 cm," represents a sample removed from the interval between 80 and 85 cm below the top of Section 5 of the second RCB core from Hole C0012G, during Expedition 333 (Fig. **F1**).

Core handling

The following sections describe in detail the flow of core from the drill floor through the laboratory. See Figure **F2** for a step-by-step flow chart of the entire process.

Core cutting area

As soon as a core is retrieved on deck, the core catcher is delivered to the core cutting area. A sample is taken for paleontological analysis, and the remainder of the core catcher sample is packed into the core liner and curated. The whole core is delivered to the core cutting area and curated for recovery length. Sections for time-sensitive whole-round samples are immediately cut out of the core, curated, and delivered to the X-ray CT laboratory for CT scanning. The time-sensitive whole-round samples include those for interstitial water and/or deep biosphere analysis. Oversight by a structural geologist in the X-ray CT laboratory acting as a "watchdog" (see below) is required before the time-sensitive whole round is pro-

cessed. If the watchdog finds a potentially high interest feature or the sample is considered inappropriate for it's intended use, Co-Chief Scientists make a decision whether or not the section may be processed. If rejected, the section is returned to the regular core flow.

Remaining core is cut into sequentially numbered 1.4 m long sections in the core cutting area. If cores contain gas in void spaces, void gas samples are collected at this time. Small (5 cm^3) plugs of sediment are removed from the bottom of appropriate core sections, typically adjacent to a whole-round sample for interstitial water squeezing, for headspace gas analysis.

The recovered core length and the total length of void space are measured, and core identification, length, drilling advance, and depth information are entered into the J-CORES database. Each section is then sealed at the top (blue cap, blue tape) and bottom (clear cap, white tape); yellow caps indicate removed whole-round core samples (with sample code marked on the end cap). All sections are marked and labeled, data are entered into the J-CORES database, and sections are moved to the core processing deck.

Core processing deck

All sections are scanned using X-ray CT, and each shift has a structural geologist acting as a watchdog to oversee the collection and selection of whole-round core samples, to identify sections or intervals of special interest or unique character, and to prevent destruction of any critical samples.

Following X-ray CT scanning and time-sensitive whole-round core sampling, core sections are allowed to equilibrate to ambient laboratory temperature (2–3 h, ~20°C), after which they are run through the whole-round multisensor core logger (MSCL-W). During Expedition 333, measurements of gamma ray attenuation (GRA) bulk density, *P*-wave velocity, resistivity, magnetic susceptibility, and natural gamma radiation were collected using the MSCL-W. Thermal conductivity measurements were also made on whole-round core sections for soft-sediment cores.

Following MSCL-W and thermal conductivity measurement, if conducted on whole-round cores, a second round of whole-round core sampling for shore-based geotechnical and hydrogeologic analyses is conducted. The number of whole-round samples collected and their locations were based on length of core recovered and extent of intact undeformed pieces from examination of the X-ray CT data.

Following completion of whole-round core sampling, sections are split axially into working and archive halves. The archive half is subjected to nondestructive color spectroscopy, digital photo image scanning, and visual core description (VCD), after which it is covered in plastic film, shrink-wrapped in plastic, and stored in either the cold-store refrigerator or the refrigerated containers at 4°C. The working half is subjected to structural analysis and sampling and measurement for physical properties (e.g., moisture and density [MAD] and velocity) and is then sampled for postcruise analyses. Following completion of sampling, these sections are also wrapped, sealed, and stored at 4°C in preparation for shipping to the core repository. All samples collected are labeled, packaged, stored, and shipped to their final destinations according to standard practice or special instructions.

Community whole-round samples

Through NanTroSEIZE expeditions, we collect substantial numbers of "community" archive samples, especially whole rounds. In some cases, these community samples will augment and/or provide redundancy for those requested by shipboard scientists. The goal is to preserve samples for a wide range of overall science objectives over the duration of the NanTroSEIZE project. This strategy, for example, will enable additional analyses of critical intervals once those zones are identified from initial shore-based laboratory tests.

During Expedition 333, each community whole-round sample was a total of 23 cm long. A community whole round was taken from each core that had sufficient recovery. The sample was cut into two pieces; one is 15 cm long, and the other is 8 cm long. These samples were shipped to Kochi Core Center (KCC) and will be made available to the NanTroSEIZE community. A "cluster" sample was associated with each community whole round.

Sample clusters

To ensure achievement of overall NanTroSEIZE scientific objectives, it is essential to collocate suites of complementary data types for integration and analysis. This must be done with appropriate and consistent sample spacing throughout each hole. During Expedition 333, sample clusters were located immediately adjacent to all whole-round intervals extracted for interstitial water geochemistry and frictional/geotechnical/hydrogeology tests, including community whole rounds. The cluster samples were taken immediately after cutting the whole-round sample. This group of samples consists of material for shipboard X-ray diffraction (XRD), MAD, carbonate analyses, X-ray fluorescence (XRF), and personal samples (e.g., grain size, fabric, and clay mineral XRD).

Routine microbiological sampling

During Expedition 333, routine microbiological sampling was conducted as per Science and Technology Panel Recommendation 0908-09 (www.iodp.org/stp/). Whole-round samples were taken when recovery was good from an interval adjacent to a whole-round sample for interstitial water and was immediately frozen at –80°C.

Where possible, samples (~1 cm^3) were removed from the top or bottom of the whole-round sample in an anaerobic glove box. The sample was put into a centrifuge tube with 9 mL of 2% paraformaldehyde fixative. After incubation at 4°C for 4–6 h, the sample was pelleted by centrifuging tubes at 3500 rotations per minute for 10 min (at 4°C) and rinsed with phosphate-buffered saline (PBS) and ethanol. The sample was stored at 4°C until it was shipped to KCC.

X-ray computed tomography

X-ray computed tomography (CT) imaging provided information about structures and sedimentological features in the core and helped to assess sample locations and quality for whole-round samples. Our methods followed those in the measurement manual prepared by the Center for Deep Earth Exploration (CDEX) (X-ray CT Scanning, version 1.00, 26 Dec 2008) and used on previous expeditions (e.g., IODP Expeditions 315, 316, 319, 322, and 331). The manual is based on GE Healthcare (2006), Mees et al. (2003), and Nakano et al. (2000).

A LightSpeed Ultra 16 (GE Yokogawa Medical Systems, Ltd.), capable of generating sixteen 0.625 mm thick slice images every 0.5 s, the time for one revolution of the X-ray source around the sample (Table T1), is the X-ray CT scanner on the *Chikyu*. Data generated for each core consist of core-axis-normal planes of X-ray attenuation values with dimensions of 512 × 512 pixels. Data were stored as Digital Imaging and Communication in Medicine (DICOM) formatted files.

Background

The theory behind X-ray CT has been well established through medical research and is very briefly outlined here. X-ray intensity varies as a function of X-ray path length and the linear attenuation coefficient (LAC) of the target material as

$$I = I_0 \times e^{-\mu L}, \quad (1)$$

where

I = transmitted X-ray intensity,
I_0 = initial X-ray intensity,
μ = LAC of the target material, and
L = X-ray path length through the material.

LAC is a function of the chemical composition and density of the target material. The basic measure of attenuation, or radiodensity, is the CT number given in Hounsfield units (HU) and is defined as

$$\text{CT number} = [(\mu_t - \mu_w)/\mu_w] \times 1000, \quad (2)$$

where

μ_t = LAC for the target material, and
μ_w = LAC for water.

The distribution of attenuation values mapped to an individual slice comprises the raw data that are used for subsequent image processing. Successive 2-D slices yield a representation of attenuation values in 3-D voxels.

Analytical standards used during Expedition 333 were air (CT number = –1000), water (CT number = 0), and aluminum (2477 < CT number < 2487) in an acrylic core mock-up. All three standards were run once daily after air calibration. For each standard analysis, the CT number was determined for a 24.85 mm^2 area at fixed coordinates near the center of the cylinder.

X-ray CT scan data usage

X-ray CT scans were used during Expedition 333 to

- Examine 3-D features of deformation structures, bioturbation, and so on;
- Distinguish "natural" fracture/faults and drilling-induced fractures;
- Measure dip angles of structures such as faults, bedding, veins, and so on;
- Provide an assessment of core and core liner integrity;
- Determine locations for whole-round samples; and
- Identify important structural and sedimentological features to be avoided by whole-round sampling.

X-ray CT scanning was done immediately after core cutting for time-sensitive (interstitial water, microbiology, and organic geochemistry) samples to finalize their selection. All whole-round core sections were screened to avoid destructive testing on intervals that may contain interesting structural or sedimentological features. This also facilitated identifying intervals with minimal drilling disturbance for whole-round sampling and for assessing heterogeneity (essential for postexpedition studies of frictional, geotechnical, and hydrogeological properties).

Lithology

Visual core descriptions

For the visual description of sediment core sections, we followed the conventional Ocean Drilling Program (ODP) and IODP procedures for recording sedimentologic information (Mazzullo and Graham, 1988). VCD forms were compiled on a section-by-section basis. Hand-written core descriptions were transferred to section-scale templates using J-CORES software and then converted to core-scale depictions using Strater software. Sediment texture (defined by the relative proportions of sand, silt, and clay) follows the classification of Shepard (1954). The classification scheme for siliciclastic lithologies follows Mazzullo et al. (1988). The Graphic lithology column on each VCD plots to scale all beds that are at least 2 cm thick. Graphic patterns do not show persistent interbedded layers <2 cm thick. These thinner layers are identified as laminae or color banding in the Sedimentary structures column.

In practice, it was difficult to discriminate between the dominant lithologies of silty clay, clayey silt, and clay without undertaking quantitative grain size analyses on board. Nevertheless, we tried to make a qualitative visual distinction between silty clay, clay, and silt on the basis that clay contains <25% silt (Shepard, 1954). The dividing line between more heavily indurated examples of the same lithologies (e.g., silty clay versus silty claystone) is arbitrary. For the inputs sites, Expedition 322 Scientists (2010), therefore, used terms for lithified rock because they only obtained RCB cores. However, since Expedition 333 also recovered HPCS and ESCS cores from the upper nonlithified stratigraphic sections at IODP Sites C0018, C0011, and C0012, this approach was not applicable and we used qualitative observational criteria to distinguish induration degree, while also consulting information from logging while drilling (at Site C0011) and physical properties data. Figure **F3** displays graphic patterns for all sedimentary lithologies encountered during Expedition 333. Also shown are symbols for internal sedimentary structures, soft-sediment deformation structures, and severity of core disturbance, for the description of which, we also consulted X-ray CT images (see **"X-ray computed tomography"**).

Where calcareous sediments occur, we used the term "calcareous mudstone" for mud deposits that contain 10%–50% calcite (following the classification Mizutani, Saito, and Kanmera, 1987) and "lime mudstone" for mud-supported fabric with >90% carbonate component (Dunham, 1962; expanded by Embry and Klovan, 1972).

To emphasize the differences in the composition and grain size of volcaniclastic material, we modified the classification scheme of Fisher and Schmincke (1984). In general, coarser grained sediments (63 µm to 2 mm average grain size) are named siliciclastic "sand" where volcaniclastic components are <25% of the total clasts. Volcaniclastic grains can be (1) reworked and commonly altered heterogeneous fragments of preexisting volcanic rock, tuff, or tephra or (2) fresh, or less altered, compositionally homogeneous pyroclasts. Pyroclasts are produced directly by many types of processes associated with volcanic eruptions, without reference to the causes of the eruption or origin of the particles. Pyroclasts can include crystals, glass shards, and rock fragments. If the sediment contains >25% but <75% volcaniclasts with a predominant grain size approaching that of sand, it is designated a "volcaniclastic sand/sandstone." If the total clast composition is >75% pyroclasts, then the sediment is classified as "ash." Depending on the grain size and degree of compaction, the nomenclature is adjusted accordingly (e.g., tuff versus ash and coarse sand-size ash versus fine silt-size ash). Because of the qualitative nature of the descriptions, compositions close to the dividing lines of the classification scheme are challenging to the interpreters. In addition, with the exception of fresh glass shards in the population of pyroclasts, it is difficult to use smear slides (see below) to discriminate unequivocally between primary eruptive products (crystals, glass shards, or rock fragments) versus particles of identical composition created by subaerial or subaqueous erosion of fresh volcanic materials. On stratigraphic columns, we therefore use the term ash as a general descriptive term for all volcaniclastic sediments and depict coarse ash beds with longer lines than fine ash beds.

Bioturbation intensity in deposits was estimated using the following semiquantitative ichnofabric index:

- Slight bioturbation = <33% of original bedding disturbed.
- Moderate bioturbation = 33%–66% of original bedding disturbed.
- Intense bioturbation = >66% of original bedding disturbed.

Separating slightly and moderately bioturbated mud may, in some cases, be biased by the smoothness of the section surface. The ichnofabric index in cores was identified with the help of visual comparative charts (Heard et al., 2008).

Smear slide description

Smear slides are useful for identifying and reporting basic sediment attributes (texture and composition).

Results are only semiquantitative. Errors can be large, especially for textural estimates of the fine silt and clay-size fractions. Smear slide analysis also tends to underestimate the amount of sand-size grains because they are difficult to incorporate evenly onto the slide. As during Expeditions 315, 316, and 322, we suspect that the counting errors can be considerable (e.g., "Lithology" in Expedition 315 Scientists, 2009) and easily as high as ~20%.

We estimated the texture of the sediments with the help of a visual comparison chart (Rothwell, 1989). The various sediment components were divided into several categories (e.g., feldspar, pyroxene, metamorphic lithic fragments, sedimentary lithic fragments, etc.) and grouped into descriptive categories according to the following classification (Figs. F4, F5):

D = dominant (>50% of total grains).
A = abundant (>20%–50% of total grains).
C = common (>5%–20% of total grains).
P = present (>1%–5% of total grains).
R = rare (0.1%–1% of total grains).
T = trace (<0.1% of total grains).

This classification was used to optimize the reproducibility of results among different scientists. For fine-grained sediments (silt/siltstone and silty clay/claystone), rough estimations were made regarding the matrix, using the visual comparison chart after Rothwell (1989). Detailed results are summarized in the smear slides (see "Core descriptions").

The sample location for each smear slide was entered into J-CORES with a sample code of "SS," using the Samples application. The position of each specimen is shown on the VCD slide editor column of the VCD application. In addition, the relative abundance of some of the major components (e.g., quartz) was also validated by bulk powder XRD (see "X-ray diffraction"), and the absolute weight percent of carbonate was verified by chemical analysis (see "Organic geochemistry").

X-ray diffraction

We completed routine XRD analyses of bulk powders using a PANalytical CubiX PRO (PW3800) diffractometer. Our principal goal was to estimate relative weight percentages of total clay minerals, quartz, feldspar, and calcite using peak areas. Most of the samples were selected from intervals adjacent to whole-round samples, and most are part of sampling clusters colocated with physical properties, carbonate, and XRF. A few additional samples were collected periodically from such unusual lithologies as carbonate-cemented claystone and volcanic ash. Samples were freeze-dried, crushed with a ball mill (along with powder for XRF and carbonate), and mounted as random bulk powders.

The instrument settings were as follows:

Generator = 45 kV and 40 mA.
Tube anode = Cu.
Wavelength = 1.54060 Å ($K_{\alpha1}$) and 1.54443 Å ($K_{\alpha2}$).
Step spacing = 0.005°2θ.
Scan step time = 0.648 s.
Divergent slit = automatic.
Irradiated length = 10 mm.
Scanning range = 2°2θ to 60°2θ.
Spinning = yes.

To match ODP Leg 190, NanTroSEIZE Stage 1 expeditions, and Expedition 322 as closely as possible, MacDiff 4.2.5 software was used for data processing. The software can be acquired at: (www.ccp14.ac.uk/ccp/web-mirrors/krumm/macsoftware/macdiff/MacDiff.html). Each peak's upper and lower limits were adjusted following the guidelines shown in Table T2. Calculations of relative mineral abundance utilized a matrix of normalization factors derived from integrated peak areas and singular value decomposition (SVD) (Table T3). These SVD normalization factors for NanTroSEIZE were recalculated during Expedition 315 after the diffractometer's high-voltage power supply was replaced. To help illustrate, a computation for the "absolute" percentage of quartz in a given specimen would be (see also Table T3)

(Area clay peak × –1.5889532E–04) +
(Area quartz peak × 5.8782392E–04) +
(Area feldspar peak × –4.2840613E–05) +
(Area calcite peak × 3.3021188E–06). (3)

As thoroughly described by Fisher and Underwood (1995), calibration of SVD factors depends on the analysis of known weight-percent mixtures of mineral standards that are appropriate matches for natural sediments. Bulk powder standards for the NanTroSEIZE project are the same as those reported by Underwood et al. (2003): quartz (Saint Peter sandstone), feldspar (Ca-rich albite), calcite (Cyprus chalk), smectite (Ca montmorillonite), illite (Clay Mineral Society IMt-2, 2M1 polytype), and chlorite (Clay Mineral Society CCa-2). The Expedition 322 Scientists (2010) published examples of diffractograms for all of the standard mixtures.

If a natural mineral mixture generates peak areas close to those of the standards, then the sum of the four "absolute" percentages will be close to 100%. In practice, all of the values must be normalized such that total clay minerals + quartz + feldspar + calcite = 100%. If trace quantities of a mineral or minerals generate peaks with low intensity, use of negative

SVD normalization factors may result in computed values of absolute weight percent that are negative. This is a common problem with calcite. In such cases, we inserted the numerical value of 0.1% as a proxy for "trace."

Average errors (SVD-derived estimates versus true weight percent) needed to be recalculated during Expedition 333, so the 14 standard mineral mixtures were run three times each. This test provides a measure of operator bias for choosing the lower and upper limits of each peak (Table T2). The average precision (standard deviation) based on three analyses of each standard mixture is: total clay minerals = 1.6%, quartz = 1.2%, feldspar = 0.8%, and calcite = 1.0%. The average accuracy (true wt%–calculated wt%) is: total clay minerals = 4.3%, quartz = 2.4%, feldspar = 1.8%, and calcite = 2.2%.

In spite of its precision with standard mixtures, the SVD method is only semiquantitative, and results for natural specimens should be interpreted with some caution. One of the fundamental problems with any bulk powder XRD method is the difference in peak response between poorly crystalline clay minerals at low diffraction angles and highly crystalline minerals at higher diffraction angles (e.g., quartz and plagioclase). Contents of clay minerals are best characterized by measuring the peak area, whereas peak intensity may be easier and more accurate to quantify quartz, feldspar, and calcite. Analyzing oriented aggregates enhances basal reflections of the clay minerals, but this step is time consuming and requires isolation of the clay-size fraction to be effective. Errors also propagate as more minerals and peaks are added to the procedure. Counts for "plagioclase" may also include K-feldspar, so we refer to that value in natural specimens as "feldspar." For clay mineral assemblages, the two options are to individually measure one peak for each mineral and add the estimates together (thereby propagating the error) or to measure a single composite peak that extends from 19.4° to 20.4°2θ. Chlorite does not contribute to this composite peak, so errors grow if natural mixtures contain abundant chlorite. Another source of error is contamination of mineral standards by impurities such as quartz (e.g., the illite standard contains ~20% quartz).

In the final assessment, calculated values of a mineral's weight percent should only be regarded as relative percentages within a four-component system, where total clay minerals + quartz + feldspar + calcite = 100%. How close those estimates are to their absolute percentages within the mass of total solids will depend on the abundance of amorphous solids (e.g., biogenic opal and volcanic glass), as well as the total of all other minerals that might occur in minor or trace quantities. For most natural samples, the absolute errors are probably between 5% and 10%. Thus, the primary value of bulk powder XRD data should be to identify spatial and temporal trends in sediment composition.

X-ray fluorescence

Whole-rock quantitative XRF spectrometry analysis was undertaken on core samples for the major elements. Analyses were performed on samples of 10 cm^3 taken from every interstitial water cluster sample. Additional samples were collected from the working half of the core, usually next to samples for XRD and carbonate analysis, from unusual lithologies such as ash.

Collected samples were first vacuum-dried at least 24 h and crushed to fine powder with a tungsten carbide-ball mill. Loss on ignition was measured using weight changes on heating at 105°C for 2 h and then at 1000°C for 3 h. Glass beads were created for XRF analyses by fusing 0.9 g of sample with 4.5 g of SpectromeltA12 flux and 3 drops of LiI 20 wt% in a Pt crucible for 7 min at 1150°C. Analyses were performed on the wavelength dispersive XRF spectrometer Supermini (Rigaku) equipped with a 200 W Pd anode X-ray tube at 50 kV and 4 mA.

Major elements were measured using the fused glass bead method and are presented as weight percent oxide proportions (Na_2O, MgO, Al_2O_3, SiO_2, P_2O_5, K_2O, CaO, TiO_2, MnO, and Fe_2O_3). Rock standards of the National Institute of Advanced Industrial Science and Technology (Geological Survey of Japan [GSJ]) were used as the reference materials for quantitative analysis. Processed data were uploaded into J-CORES as a comma-delimited data file. Data are reported as total counts on the peak and also as semi-quantitative oxide weight percents.

X-ray fluorescence scanning

Semi-quantitative XRF scanning was undertaken for major elements on split-core sections using the onboard JEOL TATSCAN-F2 energy dispersive spectrometry split-core scanner, equipped with a cryogenic Si semiconductor and a 76 mm beryllium window. Target for X-ray generation is rhodium (Rh) and the diameter of the collimator that directs the incident X-ray beam is 7 mm. Prior to scanning, split-core surfaces were carefully cleaned with a brush. Core sections were scanned with a 2 cm sampling step at 30 kV (0.17 mA), with a 40 s sampling time.

Semi-quantitative oxide weight percents for major elements (Na_2O, MgO, Al_2O_3, SiO_2, P_2O_5, K_2O, CaO, TiO_2, MnO, and Fe_2O_3) were calculated from background-corrected integrated peak intensities using

software provided by the vendor (JEOL) for the TATSCAN. Processed data were uploaded into J-CORES as a comma-delimited data file. Data are reported as semi-quantitative oxide weight percents with a precision of the order of several weight percents. Therefore, results should be carefully interpreted for quantitative discussion. Data presented in "Lithology" in the "Site C0011" chapter and "Lithology" in the "Site C0012" chapter (Expedition 333 Scientists, 2012a, 2012b) was further calibrated using JB-1b reference material values measured the day of the analysis (Table T4).

Structural geology

Our methods for documenting the structural geology of Expedition 333 cores largely followed those given by the Expeditions 315, 316, 319, and 322 structural geologists (see the "Structural geology" sections in Expedition 315 Scientists [2009], Expedition 316 Scientists [2009], Expedition 319 Scientists [2010], and Expedition 322 Scientists [2010]). We documented the deformation observed in the split cores by classifying structures, determining the depth extent, measuring orientation data, and recording kinematic information. The data were hand-logged onto a printed form at the core table and then typed into both a spreadsheet and J-CORES. Where possible, the orientation data were also corrected for rotation related to drilling on the basis of paleomagnetic declination and inclination information.

Core description and orientation data collection

Each structure was recorded manually on a structural description sheet modified from that used during Expedition 322 (Fig. F6). We found that this modified sheet is particularly useful to record orientation data for linear structures (e.g., striation on the fault plane). Core measurements were based on previous ODP procedures developed during ODP/IODP expeditions in the Nankai accretionary margin, where we used plastic and metal protractors for orientation measurements (Fig. F7). During Expedition 333, we used the X-ray CT images of unsplit cores to identify structures and recognize 3-D geometry and distribution of structures, as examined during Expedition 322. Using the working half of the split core provided greater flexibility in removing (and cutting, if necessary) pieces of the core for more careful observation and measurement.

Orientations of planar and linear features in cored sediments were determined in the framework of the core coordinate system, which consists of *x*-axis to the "double line" marked on the working half, *z*-axis parallel to the core longitudinal axis to the bottom, and accordingly determined *y*-axis with the right-handed system (Fig. F8). To determine the orientation of a plane, two apparent dips of the planar feature were measured in the core coordinate system and converted to a plane represented by either a strike and dip or a dip and dip direction. This conversion was accomplished using a spreadsheet (Fig. F9). This approach had the advantage of increasing the data processing efficiency and reducing errors in transferring and retyping data (e.g., by using both R. Allmendinger's Stereonet program [www.geo.cornell.edu/geology/faculty/RWA/programs.html] and a spreadsheet). One apparent dip was typically represented by the intersection of the planar feature with the split face of the core and was quantified by measuring the dip direction and angle in the core coordinate system. Typical apparent dip measurements trended 090° or 270° and ranged in plunge from 0° to 90°. The second apparent dip was usually represented by the intersection of the planar feature and a cut or fractured surface at a high angle to the split face of the core axis. In many cases, this was a surface either parallel or perpendicular to the core axis. In the former cases, the apparent dip lineation trended 000° or 180° and plunged from 0° to 90°; in the latter cases, the trend ranged from 000° to 360° and plunged 0°. Linear features observed in the cores were always associated with planar structures (typically faults or shear zones), and their orientations were determined by measuring either the trend and plunge in the core coordinate system or the rake (or pitch) on the associated plane. All data were recorded on the log sheet with appropriate depths and descriptive information.

Paleomagnetic data were used during NanTroSEIZE to orient cores. Paleomagnetic data collection was performed on discrete cube samples from working halves (regularly two samples per section). Because the cryogenic magnetometer on the *Chikyu* was not available, structural data were systematically reoriented using average inclination and declination data of each HPCS core. Each structural measurement was reoriented for EPCS, ESCS, and RCB core only if there was an appropriate paleomagnetic data point within the same coherent interval.

Orientation data analysis based on the spreadsheet

During Expedition 333, we adopted the Expedition 315/316 spreadsheet template for orientation data calculation in the core coordinate system, as well as in the geographic coordinate system from those data measured on cores (e.g., Fig. F9).

Calculation of plane orientation

For planar structures (e.g., bedding or faults), two apparent dips on two different surfaces (e.g., one being the split core surface and the other being the horizontal surface) were measured in the core coordinate system as azimuths (measured clockwise around the *z*-axis from the *x*-axis, looking down) and plunges (Fig. F10). If the azimuths and plunges of the two apparent dips are given as (α_1, β_1) and (α_2, β_2), respectively, as in Figure F10, then the unit vectors representing these two lines, v_1 and v_2, are

$$v_1 = \begin{pmatrix} l_1 \\ m_1 \\ n_1 \end{pmatrix} = \begin{pmatrix} \cos\alpha_1 \cos\beta_1 \\ \sin\alpha_1 \cos\beta_1 \\ \sin\beta_1 \end{pmatrix}, \quad (4)$$

and

$$v_2 = \begin{pmatrix} l_2 \\ m_2 \\ n_2 \end{pmatrix} = \begin{pmatrix} \cos\alpha_2 \cos\beta_2 \\ \sin\alpha_2 \cos\beta_2 \\ \sin\beta_2 \end{pmatrix}, \quad (5)$$

where *l*, *m*, and *n* represent the *x*-, *y*-, and *z*-components of the vectors.

The unit vector normal to this plane (v_n) (Fig. F10) is then defined as follows:

$$v_n = \begin{pmatrix} l_n \\ m_n \\ n_n \end{pmatrix} = \frac{v_1 \times v_2}{|v_1 \times v_2|}, \quad (6)$$

where

$$v_1 \times v_2 = \begin{pmatrix} \begin{vmatrix} m_1 & m_2 \\ n_1 & n_2 \end{vmatrix} \\ \begin{vmatrix} n_1 & n_2 \\ l_1 & l_2 \end{vmatrix} \\ \begin{vmatrix} l_1 & l_2 \\ m_1 & m_2 \end{vmatrix} \end{pmatrix} = \begin{pmatrix} m_1 n_2 - m_2 n_1 \\ n_1 l_2 - n_2 l_1 \\ l_1 m_2 - l_2 m_1 \end{pmatrix}. \quad (7)$$

The azimuth (α_n) and plunge (β_n) of v_n are given by

$$\alpha_n = \tan^{-1}\left(\frac{m_n}{l_n}\right), \beta_n = \sin^{-1} n_n. \quad (8)$$

The dip direction (α_d) and dip angle (β) of this plane are an and 90° + β_n, respectively, when $\beta_n < 0°$ (Fig. F11A). They are $\alpha_n \pm 180°$ and 90° – β_n, respectively, when $\beta_n \geq 0°$ (Fig. F11B). The right-hand rule strike of this plane (α_s) is then given by α_d – 90° (Fig. F11).

Calculation of slickenline rake

For a fault with slickenlines, the apparent rake angle of the slickenline (ϕ_a) was measured on the fault surface from either the 090° or 270° direction of the split-core surface trace (Fig. F12). Fault orientation was measured as described above. Provided that v_n and v_c are unit vectors normal to the fault and split core surfaces, respectively, the unit vector of this intersection line (v_i) is perpendicular to both v_n and v_c (Fig. F12) and is therefore defined as follows:

$$v_i = \begin{pmatrix} l_i \\ m_i \\ n_i \end{pmatrix} = \frac{v_n \times v_c}{|v_n \times v_c|}, \quad (9)$$

where

$$v_c = \begin{pmatrix} 1 \\ 0 \\ 0 \end{pmatrix}, \quad (10)$$

and

$$v_n \times v_c = \begin{pmatrix} \begin{vmatrix} m_n & 0 \\ n_n & 0 \end{vmatrix} \\ \begin{vmatrix} n_n & 0 \\ l_n & 1 \end{vmatrix} \\ \begin{vmatrix} l_n & 1 \\ m_n & 0 \end{vmatrix} \end{pmatrix} = \begin{pmatrix} 0 \\ n_n \\ -m_n \end{pmatrix}. \quad (11)$$

Based on the right-hand rule strike of the fault plane (α_s), the unit vector (v_s) toward this direction is then

$$v_s = \begin{pmatrix} \cos\alpha_s \\ \sin\alpha_s \\ 0 \end{pmatrix}. \quad (12)$$

The rake angle of the intersection line (ϕ_i) measured from the strike direction is given by

$$\phi_i = \cos^{-1}(v_s \times v_i) \quad (13)$$

because

$$v_s \times v_i = |v_s||v_i|\cos\phi_i = \cos\phi_i, \quad (14)$$

and

$$|v_s| = |v_i| = 1. \quad (15)$$

The rake angle of the slickenline (ϕ) from the strike direction is $\phi_i \pm \phi_a$, depending on which direction the apparent rake was measured from and which direction the fault plane dips toward. ϕ_a should be subtracted from ϕ_i when the fault plane dips toward the west and ϕ_a was measured from either the top or 090°

direction (Fig. F13A) or when the fault plane dips toward the east and ϕ_a was measured from either the bottom or 090° direction (Fig. F13B). However, ϕ_a should be added to ϕ_i when the fault plane dips toward the east and ϕ_a was measured from either the top or 270° direction (Fig. F13C) or when the fault plane dips toward the west and ϕ_a was measured from either the bottom or 270° direction (Fig. F13D).

Azimuth correction using paleomagnetic data

Provided that a core is vertical, its magnetization is primary, and its bedding is horizontal, its paleomagnetic declination (α_p) indicates magnetic north where the inclination (β_p) ≥ 0° (Fig. F14A), whereas it indicates magnetic south where β_p < 0° (Fig. F14B). The dip direction and strike of a plane in the geographic coordinate system (α_d* and α_s*) are therefore

$$\alpha_d^* = \alpha_d - \alpha_p, \quad (16)$$

and

$$\alpha_s^* = \alpha_s - \alpha_p, \quad (17)$$

where

$$\beta_p \geq 0° \quad (18)$$

and are

$$\alpha_d^* = 180° + \alpha_d - \alpha_p, \quad (19)$$

and

$$\alpha_s^* = 180° + \alpha_s - \alpha_p, \quad (20)$$

where

$$\beta_p < 0°. \quad (21)$$

J-CORES structural database

J-CORES database has a VCD program to store a visual (macroscopic and/or microscopic) description of core structures at a given section index and a record of planar structures in the core coordinate system. The orientations of such features are saved as commentary notes but do not appear on the plots from the Composite Log Viewer. During Expedition 333, only the locations of structural features are entered in J-CORES, and orientation data management and planar fabric analysis are done with an Excel spreadsheet as mentioned above.

Description and classification of structures

In general, we described and classified the structures observed using the terminology of J-CORES and Expedition 315/316, which in turn is based on the J-DESC VCD scheme and ODP Legs 131 (Taira, Hill, Firth, et al., 1991), 156 (Shipley, Ogawa, Blum, et al., 1995), 170 (Kimura, Silver, Blum, et al., 1997), and 190 (Moore, Taira, Klaus, et al., 2001). For clarity, however, we define the terminology used to describe fault-related rocks, as well as the basis for differentiating natural and drilling-induced features. The key to the symbols used in J-CORES is given in Figure F3.

Biostratigraphy

Without a micropaleontologist on board during Expedition 333, a preliminary calcareous nannofossil investigation was completed by shore-based analysis during and after the cruise by sending samples from the ship. Similar in study procedure to Expedition 322, preliminary ages were assigned to sedimentary strata primarily based on core catcher samples. Samples from within the cores were examined when a more refined age determination was necessary. The biostratigraphic events, zones, and subzones for nannofossils we used are summarized in Fig. F15. The Pliocene/Pleistocene boundary has been formally located just above the top of the Olduvai (C2n) magnetic polarity subchronozone (Aguirre and Pasini, 1985) and just below the lowest occurrence of medium *Gephyrocapsa caribbeanica* (≥3.5 µm but <5.5 µm) (Takayama and Sato, 1993–1995; Raffi et al., 2006). We used the lowest occurrence of medium *G. caribbeanica* (≥3.5 µm but <5.5 µm) to mark the Pliocene/Pleistocene boundary. The Miocene/Pliocene boundary has not been formally defined yet in terms of nannofossils. We tentatively used the last occurrence (LO) horizon of *Discoaster quinqueramus* for the boundary.

Details of the methods are described as the following (zonal scheme and nannofossil biohorizons are shown in Figure F15 and Table T5):

- The calcareous nannofossil zonal scheme established by Martini (1971) and Okada and Bukry (1980) and modified by Young (1998) was used for lower Miocene–Quaternary sequences.
- The calcareous nannofossil biostratigraphic classification of sedimentary sequences follows the review by Raffi et al. (2006).
- In addition, the upper Pliocene–Quaternary biohorizons originally defined by Sato and Takayama

(1992) and modified by Raffi et al. (2006) were used for more detailed correlations.

- Astronomically tuned age estimates for the lower Miocene–Quaternary rely on the geological timescale developed by the International Commission on Stratigraphy in 2004 (Lourens et al., 2004).
- A size-defined species of the genera *Reticulofenestra* was placed into size categories as proposed by Young (1998).
- For the gephyrocapsids, we adopted the concept of Raffi et al. (2006), and morphological terminology used here is summarized in Perch-Nielsen (1985) and Takayama and Sato (1987). Accordingly, *Gephyrocapsa* is divided into four major groups by maximum coccolith length:
  - Small *Gephyrocapsa* (<3.5 µm),
  - Medium *Gephyrocapsa* (*G. caribbeanica* and *Gephyrocapsa oceanica;* ≥3.5 but <5.5 µm),
  - *Gephyrocapsa* sp. 3 (*Gephyrocapsa parallela;* ≥4 µm but <5.5 µm), and
  - Large *Gephyrocapsa* (*G. caribbeanica* and *G. oceanica;* ≥5.5 µm).

Methods

For nannofossil analyses, the core catcher sections of each core were sampled. Samples from other sections were sometimes included where nannofossils were not abundant in core catcher material, and many such samples were targeted specifically in burrows. Standard smear slide methods were utilized for all samples using optical adhesive as a mounting medium. We followed the taxonomic concepts summarized in Takayama and Sato (1987).

Calcareous nannofossil preservation was based on the following:

G = good (little or no evidence of dissolution and/or overgrowth).
M = moderate (minor dissolution or crystal overgrowth observed).
P = poor (strong dissolution or crystal overgrowth, many specimens unidentifiable).

Total abundance of calcareous nannofossils for each sample was estimated as

A = very abundant (>50 specimens per field of view [FOV]).
C = common (>10–50 specimens per FOV).
F = few (>1–10 specimens per FOV).
R = rare (1 specimen per 2 or more FOVs).

Nannofossil abundances of individual species were recorded as

A = abundant (1–10 specimens per FOV).
C = common (1 specimen per 2–10 FOVs).
R = rare (1 specimen per >10 FOVs).

Paleomagnetism

Paleomagnetic and rock magnetic investigations on board the *Chikyu* during Expedition 333 were primarily designed to determine the characteristic remanence directions for use in magnetostratigraphic and tectonic studies. Routine measurements on archive halves could not be conducted because the superconducting rock magnetometer was being repaired at the factory and a system was being upgraded during this expedition. Paleomagnetic measurements were thus only performed on discrete sediment and sedimentary rocks and basalts (~2.2 cm cubes of 7 cm^3) taken from the working halves using spinner magnetometers as described below. Before the paleomagnetic measurements were taken, bulk magnetic susceptibility was measured.

Spinner magnetometer

Two spinner magnetometers, models SMD-88 and ASPIN (Natsuhara Giken Co., Ltd.), were utilized during Expedition 333 for remanent magnetization measurement. They were installed in a large magnetically shielded room (7.3 m × 2.8 m × 1.9 m) in the paleomagnetism laboratory. The total magnetic field in this room is ~1% of Earth's magnetic field. One magnetometer (ASPIN) was borrowed from the Institute for Research on Earth Evolution (IFREE), Japan Agency for Marine-Earth Science and Technology (JAMSTEC) for this expedition.

The spinner magnetometers can measure magnetization from 5×10^{-6} to 3×10^{-1} mAm^2 with noise levels of ~5×10^{-7} mAm^2. Sediments collected during this expedition were measured using a short-type holder for the 7 cm^3 cube samples. Basalt rocks were measured using a tall-type holder for a 7 cm^3 sample. The samples were measured in six different positions with data stacking of usually 10 or 20 spins and sometimes up to 64 spins, depending on the intensity of samples.

Alternating-field demagnetizer

Two alternating-field (AF) demagnetizers, DEM-95C and DEM-95 (Natsuhara Giken Co., Ltd.), were set for demagnetization of 7 cm^3 discrete samples of sediment and sedimentary rocks (DEM-95 was borrowed from IFREE, JAMSTEC). The units are equipped with a sample tumbling system for AF demagnetization (maximum AF = 180 mT). The samples were demagnetized using these instruments to decipher paleomagnetic data from samples. There are various different magnetic components in samples, so stepwise AF demagnetizations were performed at five steps (Natural remanent magnetization, 5, 10, 20, and 30 mT)

after remanent magnetization was measured. We carried out extra steps on a few selected samples to assess their magnetic characteristics in detail.

Thermal demagnetizer

The thermal demagnetizer TDS-1 (Natsuhara Giken Co., Ltd.) has a single chamber for thermal demagnetization of dry samples over a temperature range from room temperature to 800°C. The chamber holds up to 8 or 10 cubic or cylindrical samples, depending on the exact size. The oven requires a closed system of cooling water, which is conveniently placed next to the shielded room. A fan next to the µ-metal cylinder that houses the heating system is used to cool samples to room temperature. The measured magnetic field inside the chamber is <20 nT. Representative samples were step-wisely heated to determine magnetic components and their unblocking temperatures.

Magnetic susceptibility measurement system

Bulk magnetic susceptibility was measured using the Kappabridge KLY 3S (AGICO Inc.), designed for anisotropy of magnetic susceptibility (AMS) measurements. Sensitivity, intensity, and frequency of field applied for AMS measurements are 2×10^{-8} SI, 300 mA/m, and 875 Hz, respectively.

Coordinate geometry of the samples

Two discrete cube samples (7 cm^3) were taken for each section from the working halves. Sampling intervals are dependent on core conditions (e.g., to avoid flow-in, coring disturbances, etc.). The samples were selected carefully from undisturbed hemipelagic mud(stone) layers. Coordinate geometry of the sample is shown in Figure **F16.**

Paleomagnetic reorientation of cores

Azimuthal orientation of drilled cores is of prime importance when modeling directional properties of rock formations. Paleomagnetic core reorientation has been successfully used for a number of years (e.g., Fuller, 1969; Kodama, 1984; Shibuya et al., 1991). The procedure is based on determining the direction of stable remanent magnetization (either viscous remanent magnetization or primary magnetization) with respect to a common reference line that is scribed lengthwise along the core.

Magnetic reversal stratigraphy

Magnetic polarity was determined based on inclination. Sites C0011, C0012, and C0018 are at latitudes 32°50′N, 32°45′N, and 33°09′N, which translates into expected inclinations of 52.2°, 52.1°, and 52.6°, respectively. This inclination is steep enough to distinguish the magnetic polarities (normal or reversed) on the sign of the magnetic inclination (positive or negative) for at least Neogene and Quaternary sediments, even with the expected tectonic latitudinal migration. Zijderveld plots were inspected visually for behavior of remanent magnetization after demagnetization. Stable (primary) remanent magnetization directions of discrete samples were fit using principal component analysis (Kirschvink, 1980), and the obtained inclination was used for the determination of paleomagnetic field polarity.

Geomagnetic polarity reversals are well dated and globally synchronous geophysical phenomena. Magnetostratigraphy is a well-proven tool for precise temporal correlation and accurate dating in sediments. During this expedition, magnetozones were recognized on the basis of distinct intervals of magnetic reversal zones, also taking into account tephrochronologic and biostratigraphic data. Normal polarity subchrons are referred to by adding suffixes (n1, n2) that increase with age. For the younger part of the timescale (Pliocene–Pleistocene), we use traditional names to refer to the various chrons and subchrons (e.g., Brunhes, Jaramillo, etc.). In general, polarity reversals occurring at core ends have been treated with extreme caution. The ages of the polarity intervals used during this expedition are the same as those for Expeditions 315, 316, and 322, which is the magnetostratigraphic timescale for the Neogene by Lourens et al. (2004) (Table **T6**).

For calcareous nannofossil zonations, Raffi et al. (2006) was used as a standard timescale for the entire NanTroSEIZE, including this expedition (see **"Biostratigraphy"**). This timescale relies on ATNTS2004 (Lourens et al., 2004). Although the magnetostratigraphic timescale on figures in Raffi et al. (2006) incorporated slight modifications to ATNTS2004, there is no clear explanation with an appropriate table for these modifications. Because of this and the fact that there is no significant change affecting the main chron boundaries, we used ATNTS2004 (Lourens et al., 2004) to keep consistency within NanTroSEIZE expeditions. However, we need to note that the boundary ages for Chron C5ABn listed as "13.252-13.466 C5ABn" in the geomagnetic polarity timescale (GPTS) table used for Expeditions 315 (Expedition 315 Scientists, 2009, table T7) and 316 (Expedition 316 Scientists, 2009, table T10) should be replaced with the correct values of 13.369 (top) and 13.605 (bottom) according to Lourens et al. (2004) because they are using the same timescale. For the up-to-date Neogene GPTS for reference, we need to

consider the discussion by Hilgen (2008), especially for Chrons C7n through C5Cn.1n between 24.1 and 15.9 Ma and for chron boundaries in the interval between 12.5 and 8.5 Ma. These might be included in the shore-based study and for future NanTroSEIZE expeditions.

Data reduction and software

Data reduction (Zijderveld demagnetization plots and Schmidt net projections) was conducted using visualization software called "Progress" installed on the PC controlling the spinner magnetometers. Principal components were analyzed using Progress to determine characteristic remanent magnetization directions based on Kirschvink (1980).

Physical properties

Physical property measurements provide valuable constraints on bulk physical character to augment lithologic unit characterization and to facilitate correlation of seismic reflection data with discrete core measurements and core descriptions. Thus, these data provide information necessary for reliable core-seismic integration. Expedition 333 employed multiple approaches and methods to characterize the physical properties of cores. Prior to core physical property measurements, X-ray CT images were collected for all cores, and cores were equilibrated with room temperature (~20°C). After temperature equilibration, whole-round core sections were processed in the whole-round multisensor core logger (MSCL-W) to measure gamma ray attenuation (GRA) density, magnetic susceptibility, natural gamma radiation, *P*-wave (compressional) velocity, and electrical resistivity. For cores with soft, unconsolidated sediments, thermal conductivity was measured using a TeKa thermal conductivity meter with the VLQ full-space needle probe inserted in whole-round cores after MSCL-W measurements. Cores were then split into archive and working halves. For cores with lithified sediments, a needle probe could not be inserted, thermal conductivity measurements were made on working halves using the TeKa thermal conductivity meter in half-space mode (HLQ). Discrete samples were collected from the working halves for moisture and density (MAD) measurements. Specimen mass was taken with a BAL-2 motion-compensated shipboard balance system. The volume of solids was measured with a Quantachrome penta-pycnometer. For soft sediments, undrained shear strength at discrete intervals from the working halves was determined from vane shear measurements made with a Wykeham Farrance WF23544 vane apparatus and penetrometer measurements made with a Geotest E-284B penetrometer. Resistivity was measured on soft-sediment cores using a Wenner array of electrodes and an impedance meter. *P*-wave velocity and electrical resistivity were measured on discrete core samples in the *x*-, *y*-, and *z*-directions when sediments were hard enough to permit samples to be taken. Details and procedures for each physical property measurement are described below.

For basalt samples, modified procedures were used. If recovery allowed, one sample per core was cut to be used for *P*-wave velocity and electrical resistivity. After cutting, this sample was soaked in 35 g/L NaCl solution under vacuum for 24 h prior to measurement. After measurement, this sample was used for paleomagnetic analyses. A MAD sample was obtained from the same interval as the *P*-wave and electrical resistivity sample. It was soaked under vacuum for 24 h. After soaking, the outer surface of the sample was blotted to remove surficial water. It then followed typical MAD procedures described below. Because of the limited size of the available vacuum chamber, samples for thermal conductivity could not be soaked under vacuum prior to measurement. Instead, the sample was obtained as soon as practical after the core was split and soaked in 35 g/L NaCl solution for 15 min.

MSCL-W

GRA density

Bulk density can be used to evaluate pore volume in sediment, which provides information on the consolidation state of sediment. GRA density is based on the detection of a gamma ray beam produced by a cesium source. The beam, produced by a ^{137}Cs gamma ray source at a radiation level of 370 MBq within a lead shield with a 5 mm collimator, is directed through whole-round cores. The gamma ray detector includes a scintillator and an integral photomultiplier tube to record the gamma rays that pass through the whole-round core. GRA bulk density (ρ_b) is calculated as

$$\rho_b = \ln(I/I_0)\mu d, \quad (22)$$

where

I_0 = gamma ray source intensity,
I = measured intensity of gamma rays passing through the sample,
μ = Compton attenuation coefficient, and
d = sample diameter.

The Compton attenuation coefficient (μ) and source intensity (I_0) are treated as constants, so ρ_b can be calculated from I. The gamma ray detector is calibrated with a sealed calibration core (a standard core

liner filled with pure water [Elix] and aluminum cylinders of various diameters). To establish the calibration curves, gamma ray counts were taken through each aluminum cylinder for 60 s. Each aluminum cylinder has a density of 2.7 g/cm^3, and d is 1, 2, 3, 4, 5, or 6 cm. The relationship between I and μd is

$$\ln(I) = A(\mu d) + B, \quad (23)$$

where A and B are coefficients determined from the calibration experiment. GRA density measurements on core samples were conducted every 4 cm for 4 s. The spatial resolution was 5 mm.

Magnetic susceptibility

Magnetic susceptibility is the degree to which a material can be magnetized by an external magnetic field. Therefore, magnetic susceptibility provides information on sediment composition. A Bartington loop sensor with an 8 cm diameter was used to measure magnetic susceptibility. An oscillator circuit in the sensor produces a low-intensity (~80 A/m RMS), nonsaturating, alternating magnetic field (0.565 kHz). This pulse frequency is converted into magnetic susceptibility. The spatial resolution of the loop sensor is 23–27 mm, and it is accurate to within 5%. Magnetic susceptibility data were collected every 4 cm along the core.

Natural gamma radiation

Natural gamma radiation measurements provide insights into sediment composition and thus can be used to identify lithology. Whole-round cores were monitored for natural gamma ray (NGR) emissions to obtain spatial variability in radioactivity and establish gamma ray logs of cores for correlation to downhole gamma ray logs. A lead-shielded counter, optically coupled to a photomultiplier tube and connected to a bias base that supplies high-voltage power and a signal preamplifier, is used. Two horizontal and two vertical sensors are mounted in a lead, cube-shaped housing. The NGR system records radioactive decay of long-period isotopes ^{40}K, ^{232}Th, and ^{238}U. NGR has a resolution of 120–170 mm and was measured every 16 cm with a count time of 30 s. Background radiation noise was determined by taking measurements on a water-filled calibration core.

P-wave velocity

P-wave data can be used to evaluate small-strain moduli, to correlate between log and core data, and to evaluate pore structure and cementation. *P*-wave (compressional) velocity (V_P) is defined by the time required for a compressional wave to travel a set distance:

$$V_P = d/t_{core}, \quad (24)$$

where

d = path length of the wave across the core, and
t_{core} = traveltime through the core.

P-wave velocity transducers on the MSCL-W system measure total traveltime of the compressional wave between transducers. The wave travels horizontally across the whole core and core liner. The total traveltime observed is composed of

t_{delay} = time delay related to transducer faces and electronic circuitry,
t_{pulse} = delay related to the peak detection procedure,
t_{liner} = transit time through the core liner, and
t_{core} = traveltime through the sediment or rock.

The system is calibrated using a core liner filled with distilled water, which provides control for t_{delay}, t_{pulse}, and t_{liner}. With these calibrations, core velocity (V_P) can be calculated on whole-round specimens in core liners as follows:

$$V_P = (d_{cl} - 2d_{liner})/(t_o - t_{pulse} - t_{delay} - 2t_{liner}), \quad (25)$$

where

d_{cl} = measured diameter of core and liner,
d_{liner} = liner wall thickness, and
t_o = measured total traveltime.

Equation 25 assumes that the core completely fills the core liner.

Electrical resistivity

Within limits, electrical resistivity may be useful for estimating other sediment physical properties, including porosity, tortuosity, permeability, and thermal conductivity. Bulk electrical resistivity is controlled by solid grain resistivity, interstitial water resistivity, pore space distribution, and pore connectivity. Electrical resistivity (ρ) is defined by the electrical resistance and geometry of the core measured:

$$\rho = R(A/L), \quad (26)$$

where

R = electrical resistance,
L = length of measurement, and
A = cross-sectional area of the core.

The noncontact resistivity sensor on the MSCL-W system induces a high-frequency magnetic field in the core with a transmitter coil. This generates an electrical current in the bulk sediment that is inversely proportional to its resistivity. The secondary magnetic field generated by this induced electrical current is measured by a receiver coil. To measure

this smaller magnetic field accurately, a differencing technique has been developed that compares readings from the sample core to readings from an identical set of coils operating in air. Electrical resistivity data were obtained at 4 cm intervals on the MSCL-W.

Moisture and density measurements

Discrete samples from the working-half cores were used for determination of index properties (e.g., bulk density, grain density, dry density, water content, porosity, and void ratio). Index properties are determined from mass measurements on wet and dry specimens and volume measurements on dry specimens. Standard ODP/IODP practices, which include a salt correction, were used to determine interstitial water mass and volume, salt mass and volume, and solid grain mass and volume (Blum, 1997). Standard seawater density (1.024 g/cm^3) and salinity (35‰) and a constant salt density (2.22 g/cm^3) were assumed for all calculations.

In general, two discrete samples of homogeneous lithology for index properties were collected from each core section. Where whole-round samples were taken (e.g., interstitial water sample, community whole round, or individual sample requests), a MAD sample was taken adjacent to the whole-round sample as part of a cluster sample. Sample intervals and frequency were occasionally shifted to select minimally disturbed, homogeneous samples. Lithology was noted where it was visibly distinct from clay or silt, such as samples dominated by sand or ash.

Wet and dry masses were measured using a paired electronic balance system, which is designed to compensate for the ship's heave. The sample mass was counterbalanced with a precisely known mass (10 g for sediment, 40 g for basalt). The sample mass was determined to a precision of ±0.01 g. The balance system was calibrated twice a day or more frequently during poor weather conditions. To minimize desiccation, MAD sample collection was followed immediately by measurement of wet sediment mass (M_{wet}). After M_{wet} measurements, samples were dried in a convection oven at 105° ± 5°C for 24 h. Dry samples were placed in a desiccator for at least 1 h to equilibrate to room temperature (~20°C), and then dry sediment mass (M_{dry}) and volume (V_{dry}) were measured. Two five-chamber Quantachrome penta-pycnometers were used to measure V_{dry} with a helium-displacement technique providing a precision of ±0.04 cm^3. The five-chamber system allowed the measurement of four sample volumes and one calibration sphere. Each measured volume (V_{dry}) is the average of five volume measurements. The calibration sphere was rotated between all measurement chambers to monitor for errors in each chamber. The pycnometer was calibrated at least once per 24 h.

Water content

Water content (W_c) was determined following the American Society for Testing and Materials (ASTM) standard D2216 (ASTM International, 1990). Corrections are required for salt when measuring the water content of marine samples. In addition to the water content calculation in ASTM D2216 (i.e., the ratio of interstitial water mass to dry sediment mass; W_c[dry]), we also calculated the ratio of interstitial water mass to total sample mass (W_c[wet]). The equations for water content are

$$W_c(\text{dry}) = (M_{wet} - M_{dry})/(M_{dry} - sM_{wet}), \quad (27)$$

and

$$W_c(\text{wet}) = (M_{wet} - M_{dry})/M_{wet}(1 - s), \quad (28)$$

where

M_{wet} = total mass of the discrete sample,
M_{dry} = mass of the dry sample, and
s = salinity (assumed constant at 0.035).

Bulk density

Bulk density is the density of the discrete core sample ($\rho_b = M_{wet}/V_t$). Total sample volume assuming 100% saturation ($V_t = V_g + V_{IW}$) was determined from the pycnometer measurement of grain volume (V_g) and calculated volume of interstitial water (V_{IW}). Solid grain and interstitial water volume are determined as

$$V_g = V_{dry} - (M_{wet} - M_{dry})s/\rho_{salt}(1 - s), \quad (29)$$

and

$$V_{IW} = (M_{wet} - M_{dry})/\rho_{IW}(1 - s), \quad (30)$$

where

V_{dry} = dry volume,
ρ_{salt} = salt density, and
ρ_{IW} = standard seawater density.

Porosity and void ratio

Porosity (ϕ) relates the volume of the pores to the total sample volume; void ratio (e) relates the pore volume to the volume of the solid grains. They are calculated as

$$\phi = \rho_b V_{IW}/M_{wet}, \quad (31)$$

and

$$e = V_{IW}/V_g. \quad (32)$$

Grain density

Grain density (ρ_g) was determined from measurements of dry mass and dry volume made with the dual-balance system and the pycnometer, respectively. Mass and volume were corrected for salt, yielding

$$\rho_g = (M_{dry} - M_{salt})/\{V_{dry} - (M_{wet} - M_{dry})s/[\rho_{salt}(1 - s)]\}, \quad (33)$$

where

M_{salt} = mass of salt.

Shear strength measurements

The undrained shear strength of soft sediments in the working half of the core was measured using an analog vane shear device (Wykeham Farrance, model WF23544) and a pocket penetrometer (Geotest E-284B). Measurements were made at discrete locations on the working halves above the depth where sediments behaved in a brittle manner, which corresponded to measurable shear strength <180 kPa. Where possible, the measurements were made near MAD samples. Care was taken to conduct tests within minimally disturbed, homogeneous sediments. Measurements were made on the working half of split cores with vane rotation axis and penetrometer penetration direction perpendicular to the *y*-*z* plane of the core.

Vane shear strength ($S_{u[v]}$) can be determined by the torque required to cause failure (T) and a vane constant (K_v):

$$S_{u[v]} = T/K_v. \quad (34)$$

All vane shear strength measurements were obtained using a vane with a height of 12.7 mm and a blade length of 6.35 mm. Failure torque was determined by measuring the rotation of a torsional spring using a spring-specific relation between rotation angle and torque. Vane shear strength results were only reliable for samples with vane shear strength <180 kPa. When cracking or core separation occurred, measurements were discarded. Below the depth where strength exceeded 180 kPa, no measurements were made.

The pocket penetrometer provides a measure of unconfined compressive strength (q_u), with units of mass per area), which can be related to undrained shear strength ($S_{u[penet]}$):

$$S_{u[penet]} = (q_u \times g)/2, \quad (35)$$

where

g = acceleration due to gravity.

Unconfined compressive strength is calculated from the penetration resistance generated by pushing a cylindrical probe with a diameter of 6.4 mm into the *y*-*z* plane of the core. The average of three adjacent penetrometer tests in intact, homogeneous sediment is the recorded unconfined compressive strength. After shear strength exceeded ~180 kPa, no penetrometer measurements were made.

P-wave velocity

P-wave velocity and electrical resistivity measurements were performed on cubic samples cut from rock cores with a diamond blade saw. Samples for *P*-wave velocity and electrical resistivity measurements were ~20 mm × 20 mm × 20 mm. All cubes were cut with faces orthogonal to the *x*-, *y*-, and *z*-axes of the core reference. This three-component measurement plan enables first-order measurement of both *P*-wave velocity and electrical resistivity anisotropies.

To measure *P*-wave velocity in a given direction, a *P*-wave logger for discrete samples (PWL-D) was used. The PWL-D has two 230 kHz transducers, one used as a transmitter and one as a receiver, and a laser distance sensor. A sample was placed between the transducers. The transmitter was connected to a pulse generator, and the receiver was connected to an oscilloscope synchronized with the pulse generator. The oscilloscope signal was displayed digitally and the *P*-wave total traveltime (t) for the first arrival was picked and recorded. The laser distance sensor provided the sample length (L). The velocity in any direction (e.g., V_{Px}) was defined by the sample length (e.g., L_x), total traveltime (t_x), and system-calibrated delay time (t_{delay}):

$$V_{Px} = L_x/(t_x - t_{delay}). \quad (36)$$

Calibration of the traveltime delay and laser distance sensor was conducted daily. Traveltime delay was determined by placing the transmitter and receiver in direct contact and measuring traveltime. The laser distance sensor was calibrated by placing the transmitter and the receiver in direct contact and then spacing them using a 2.5 cm long reference specimen. Routine quality control measurements were made by measuring velocity on glass and acrylic

standards with known lengths and acoustic velocities.

Electrical resistivity

On cores of soft sediment, an Agilent 4294A precision impedance analyzer was used to measure electrical resistivity using the four-electrode method. The measurement array consisted of four 1 cm long gold-plated electrodes spaced 7.5 mm apart. The array was inserted into the formation for the measurement. During measurement, the two outer electrodes inject an alternating current into the sample, and the two inner electrodes measure the resulting potential difference. The magnitude ($|Z|$) and phase (θ) of the complex impedance were measured at 2 kHz across the array. Electrical conductivity of the formation (σ_f) is computed from the complex impedance:

$$\sigma_f = \cos\theta/d|Z|, \quad (37)$$

where

d = geometric factor specific to the electrode array.

d was determined by comparing the measured $|Z|$ and θ of a 35 g/L NaCl solution with the known resistivity of the solution measured with a resistivity meter. A new value of d was computed every 24 h, and the temperature was recorded. This accounted for changes in electrode array geometry because of slight bending of the electrodes and corrosion. Resistivity of the formation was then computed as $1/\sigma_f$ calculated from Equation 37. The ambient air temperature was recorded at each measurement; the formation temperature was assumed to be the same as the ambient air temperature because the cores were thermally equilibrated prior to measurement.

On rock cores, resistivity was measured on discrete samples. A cube of known dimensions is held between two electrodes and impedance is measured at 2 kHz with the Agilent 4294A impedance analyzer. Sample dimensions are obtained during *P*-wave velocity measurement. The dimensions of the samples being larger than the maximum spacing between the electrodes allowed by the built-in stand, it appeared necessary to remove the upper electrode holder from the stand. It is unknown if the procedure was used during Expedition 322 to circumvent this problem. Contact between the sample and each stainless steel electrode is obtained through a filter soaked in 35 g/L NaCl solution. The impedance of the sample is obtained by subtracting the impedance of the filters from the measured impedance. The impedance of the filters is measured by stacking the two filters between the electrodes immediately after measuring the sample impedance. Sample complex conductivity for example in the *x*-direction (σ_x) is computed from measured impedance R_x and X_x by

$$\sigma_x = (L_x/L_yL_z)[(R_x - R_0) - j(X_x - X_0)/ (R_x - R_0)^2 + (X_x - X_0)^2], \quad (38)$$

where L is the length and R_0 and X_0 refer to the measured impedance of the filter. Conductivity in the *y*- and *z*-directions is obtained by substitution in Equation 38.

With *P*-wave velocity and electrical conductivity measured in the *x*-, *y*-, and *z*-directions, the anisotropy is calculated following the approach of Carlson and Christensen (1977). Some sources for anisotropy include (1) alignment of pores during consolidation, (2) fabric development due to alignment of mineral grains, and (3) microstructures such as microfractures and microcracks. The horizontal-plane anisotropy (α_{VPhor}, α_{phor}) and vertical-plane anisotropy (α_{VPvert}, α_{pvert}) calculation compares the horizontal (*x* and *y*) and vertical (*z*) components of *P*-wave velocity and conductivity expressed as a percentage of the mean:

$$\alpha_{VPhor}\,(\%) = 200[(V_{Px} - V_{Py})/(V_{Px} + V_{Py})], \quad (39)$$

$$\alpha_{VPvert}\,(\%) = 200[(V_{Px} + V_{Py})/2 - V_{Pz}]/ [(V_{Px} + V_{Py})/2 + V_{Pz}], \quad (40)$$

$$\alpha_{phor}\,(\%) = 200[(\rho_x - \rho_y)/(\rho_x + \rho_y)], \quad (41)$$

and

$$\alpha_{pvert}\,(\%) = 200[(\rho_x + \rho_y)/2 - \rho_z]/ [(\rho_x + \rho_y)/2 + \rho_z]. \quad (42)$$

In a truly transversely isotropic medium, the ratio of α_{hor} and α_{vert} for either *P*-wave velocity or resistivity is a function of the dip of foliation in the sample.

Thermal conductivity

Thermal conductivity was measured on sediment and rock samples using either the full-space needle probe (Von Herzen and Maxwell, 1959) or the half-space line source (Vacquier, 1985), which approximates an infinite line source. In soft sediments where a probe could be inserted into the core without fracturing the sediment, the full-space probe was inserted into whole-core sections through a hole drilled in the working-half side of the core liner. When sediment strength precluded use of the full-space probe or good contact between the probe and sediment was not possible, the half-space probe was used on the working half of the split core. For uncemented samples, the half-space probe was placed di-

rectly on the split core with seawater used to provide good contact. Lithified samples were placed in a seawater bath for at least 15 min before measurement with the half-space probe. Both full- and half-space measurements produce a scalar thermal conductivity value in the plane perpendicular to the orientation of the probe.

All measurements of thermal conductivity were made after the cores had equilibrated to room temperature. At the beginning of each measurement, temperature in the sediment was monitored to ensure that thermal drift was <0.4 mK/min (typically within 1–2 min). After it was established that the temperature was near equilibrium, a calibrated heat source was applied and the rise in temperature was recorded for ~80 s. Values of thermal conductivity were based on the observed rise in temperature for a given quantity of heat.

The full-space needle probe was calibrated at least once every 24 h. The calibration was performed on one of two Macor samples of known thermal conductivity (1.611 ± 2% W/[m·K], 1.623 ± 2% W/[m·K]). Calibration procedures for the half-space system are similar to those for the full-space needle probe. Half-space calibrations were made on a Macor sample of known thermal conductivity (1.652 ± 2% W/[m·K]). In addition, thermal conductivity of a water sample (0.59 W/[m·K]) was measured using a small content of gelatin mixed with water to prevent convective heat transfer, providing another calibration point for thermal conductivity values obtained by the TK04 instrument.

In situ temperature measurements

In situ temperature measurements were carried out using the advanced piston corer temperature tool (APCT-3). The APCT-3 is the third-generation tool of its kind and is used with the HPCS. The APCT-3 consists of three components: sensor logger, APCT-3 HPCS shoe, and computer software. During Expedition 333, in situ temperature measurements were taken for approximately every fourth core at Site C0018 and every second to fourth core at Sites C0011 and C0012 during HPCS coring. The temperature sensors were calibrated for a working range of 0°–55°C.

Prior to entering the hole, each instrument was held at the approximate mudline for ~10 min to equilibrate with bottom water temperature. However, the core winch depth meter was not calibrated, and site variability in measured bottom water temperature is likely due to uncertainties in depth. After bottom water temperature equilibration, the tools were lowered down the hole and penetrated the formation. The penetration of each tool into the formation causes a rise in temperature because of frictional heating. Following the initial rise in temperature, temperature decreases along a decay curve to near equilibrium. During this decay phase, it is important that the temperature tool is not disturbed. A second rise in temperature is due to frictional heating as the tool is pulled out of the formation. Temperature was measured as a time series sampled every 1 s and logged onto a microprocessor within the downhole tool; when the tool was retrieved, data were downloaded to the computer. The formation equilibrium temperature is determined based on fitting the temperature decay curve using the program TP-Fit, which runs on Matlab (M. Heeseman, pers. comm., 2007). In cases where the duration of temperature recording is short, the extrapolated formation temperature may have a large error. Therefore, a careful examination of recorded temperature time series is very important to obtain reliable data of heat flow by the method employed during this expedition.

Determination of heat flow

If heat transfer is by conduction and heat flow is constant, the thermal gradient will be inversely proportional to thermal conductivity, according to Fourier's law. This relationship can be linearized by plotting temperature as a function of cumulative thermal resistance (Bullard, 1939):

$$T(z) = T_o + q \sum_{i=1}^{N} \left(\frac{\Delta Z_i}{k(\partial)_i}\right), \quad (43)$$

where

T = temperature,
z = depth,
T_o = bottom water temperature,
q = heat flow,
$\sum_{i=1}^{N} \left(\frac{\Delta Z_i}{k(\partial)_i}\right)$ = thermal resistance, and
N = number of thermal conductivity measurements.

In practice, q and T_o are estimated by plotting $T(z)$ against cumulative thermal resistance. By using the plot of temperature versus cumulative thermal resistance, we can make an assessment of the consistency of heat flow with depth.

Inorganic geochemistry

Interstitial water collection

Interstitial water samples were obtained from 19 to 61 cm long whole-round sections. Samples were collected at a frequency of one per core when possible. Whole-round samples were cut and capped as quickly as possible after the core arrived on deck and immediately taken from the core cutting area to be

scanned by X-ray CT. A watchdog (shipboard structural geologist) viewed the composite X-ray CT scan to determine if there were structures that might warrant description and sampling from a split core. Once approved, the sediment was taken to the sample preparation laboratory and immediately extruded from the core liner into a nitrogen-flushed glove bag. Because of core expansion, the sediment could not, at times, be extruded from the core liner manually. In this situation the liner only was carefully split in the core splitting room, taking care to not disturb the sediment. Once extruded, the exterior of the whole-round sample was thoroughly cleaned with a spatula to remove drilling or liner splitting contamination, and the cleaned sediment was placed into a 9 cm diameter Manheim-type titanium squeezer (Manheim, 1966) on top of two pieces of filter paper rinsed with reagent-grade water (18.2 MΩ Millipore water) placed on two 40 mesh titanium screens. If needed, the mesh edges were wrapped with sealing tape and/or a second stack of two filter papers was placed below the mesh. Sediments were squeezed at ambient temperatures and pressures no higher than 2500 psi (17.2 MPa) to limit membrane filtration effects in clays and the release of smectite interlayer water. The interstitial water was collected into a 60 mL acid-washed plastic syringe that was attached to the bottom of the squeezer assembly. The water was then passed through a 0.45 µM disposable polytetrafluoroethylene (PTFE) filter as aliquots were distributed.

Interstitial water aliquots were collected for both shipboard and shore-based analyses (Table T7). High-density polyethylene (HDPE) sample vials for minor and trace element analysis were cleaned by immersion in 55°C 10% trace metal grade 12N HCl for a minimum of 12 h and were subsequently rinsed in Milli-Q water and dried in a class 100 laminar flow clean hood. Samples for minor and trace element shipboard analysis were acidified with optima-grade 6N HCl at least 24 h before analysis by inductively coupled plasma–atomic emission spectrometry (ICP-AES), inductively coupled plasma–mass spectrometry (ICP-MS), or major cation ion chromatography (IC). Aliquots for shore-based isotopic and transition metals analyses were stored in acid-washed HDPE bottles. Additional aliquots for analyses of oxygen, hydrogen, dissolved inorganic carbon (DIC), lithium, and chloride isotopes were placed in 2 mL septum screw-lid glass vials; samples for DIC were treated with 10 µL of a saturated $HgCl_2$ solution at room temperature. Following treatment, all interstitial water samples were stored in a 4°C refrigerator. After interstitial water extraction was complete, sediment squeeze cakes were divided and sealed in plastic bags for archive and shore-based analyses (Table T8). Sediment samples for archive and some shore-based geochemical analyses were stored in a 4°C refrigerator; all other squeeze cake samples were stored at room temperature.

Correction for drilling contamination

In many intervals, the sedimentary material was extensively fractured by drilling disturbance (see **"Inorganic geochemistry"** in the "Site C0018" chapter [Expedition 333 Scientists, 2012c]), making some interstitial water whole rounds extremely difficult to clean prior to processing. In these cases, even after thorough cleaning, the interstitial water samples were still contaminated with fluid that had circulated in the borehole during drilling operations. This is not the case with cores collected using HPCS but does occur with cores collected using EPCS, ESCS, and RCB. In continental margin sediments, the sulfate–methane transition (SMT) zone is generally reached at shallow depths in the sediment section, typically shallower than ~40 mbsf. Thus, the presence of sulfate and methane in a sample collected below the SMT may be used as an indication of drilling-induced contamination. For these cases, the sulfate concentrations measured in the samples were used to estimate the amount of drilling fluid introduced to the sample by taking the ratio of the sulfate measured in the sample to the sulfate concentration of seawater (28.9 mM). Likewise, concentration of the other ionic species were corrected based on their concentration in surface seawater using the following equation

$$X_{corrected} = [X_{measured} - (f_{sw} \times X_{sw})]/f_{IW}, \quad (44)$$

where

$X_{corrected}$ = corrected or in situ concentration of the analyte,
$X_{measured}$ = measured concentration of the analyte,
X_{sw} = element concentration in surface seawater (used in drilling),
f_{sw} = fraction of seawater introduced into the sample during drilling, and
f_{IW} = fraction of in situ interstitial water in the sample.

The fraction of seawater introduced by drilling disturbance and the fraction of in situ interstitial water are computed using the equations below:

$$f_{sw} = SO_{4\ measured}/SO_{4\ sw}, \quad (45)$$

and

$$f_{IW} = 1 - f_{sw}. \quad (46)$$

We collected a sample of the drilling fluid used during coring operations and analyzed it for all of the species measured shipboard. When a sample contained sulfate above the IC detection limit, the sulfate concentration of the drilling fluid was used to compute the amount of fluid added to the contaminated sample, which was then used to correct the other species analyzed. Both the measured and corrected interstitial water chemical concentration data are presented in the site chapters.

Interstitial water analysis

Interstitial water samples were routinely analyzed for refractive index with a RX-5000α refractometer (Atago) immediately after interstitial water extraction. The refractive index was converted to salinity based on repeated analyses of International Association of Physical Sciences of the Oceans (IAPSO) standard seawater. Precision for salinity was <0.1‰. Also, immediately after interstitial water extraction, samples were analyzed for pH and alkalinity by Gran titration with a pH electrode and a Metrohm autotitrator. Alkalinity titrations had a precision better than 0.7%, based on repeated analysis of a standard 50 µM $NaHCO_3$ solution.

Sulfate and bromide concentrations were analyzed by IC (Dionex ICS-1500) using subsamples that were diluted 1:100 with Milli-Q water. At the beginning and end of each run, several different dilutions of IAPSO standard seawater were analyzed for quality control and to determine accuracy. IAPSO standard seawater was analyzed after every seventh sample as a check for instrumental drift and to calculate analytical precision. Precision for the bromide and sulfate analyses was <5% and <3%, respectively. Average accuracy of bromide and sulfate was <0.0002% and <2%, respectively.

Chlorinity was determined via titration with silver nitrate ($AgNO_3$). We use the convention "chlorinity" for the titration data because it yields not only dissolved chloride but also all of the other halide elements and bisulfide.

Dissolved ammonium concentration was measured by colorimetry within 24 h of collecting the interstitial water sample, using an ultraviolet-visible (UV-vis) spectrophotometer (Shimadzu UV-2550) at an absorbance of 640 nm. A 0.05 or 0.1 mL sample aliquot was diluted with 1–4 mL of Milli-Q water depending on interstitial water volume, to which 0.5 mL phenol ethanol, 0.5 mL sodium nitroprusside, and 1 mL oxidizing solution (trisodium citrate and sodium hydroxide) were added in a capped plastic tube (Gieskes et al., 1991). The solution was kept in the dark at room temperature for >3 h to develop color. Precision of the ammonium analyses was <2% based on triplicate measurements of a standard solution.

Dissolved phosphate concentration was also measured by a colorimetric method using the UV-vis spectrophotometer at an absorbance of 885 nm. Because the phosphate concentration in the analysis solution must be <10 µM, appropriate aliquots of sample or standard solution (100 or 1000 µL) were diluted with 1 or 0.5 mL of Milli-Q water in a plastic tube depending on the volume of interstitial water available. The mixed color development solution (ammonium molybdate, sulfuric acid, ascorbic acid, and potassium antimonyl tartrate) was added to the tube (Gieskes et al., 1991), which was capped and kept at room temperature to develop color. Precision of the phosphate analyses was <3%.

Concentrations of major cations (sodium, potassium, magnesium, and calcium) were analyzed by IC (Dionex ICS-1500) on samples acidified with 0.4% 6M HCl. Samples were diluted by a factor of 200 with ultrapure water (18.2 MΩ). Each measurement batch included an ultrapure water blank, seven standards for calibration prepared from a commercially available cation mixed standard (Kanto Chemical Co., Inc., 07197-96), and IAPSO standard seawater (P-series) as a reference material, in addition to the interstitial water samples. IAPSO dilutions of 25%, 50%, 75%, and 100% are applied as the calibration standard. The average precision estimated by repeated measurements of ½₀₀ IAPSO standard seawater were Na^+ < 3%, K^+ < 1.5%, Mg^{2+} < 1.3%, and Ca^{2+} < 1.3%, and the average accuracy of the analyses were Na^+ < 0.2%, K^+ < 1%, Mg^{2+} < 0.2%, and Ca^{2+} < 0.08%. Because of potentially poor precision and accuracy of the sodium determination, which is typical of Na^+ analysis by IC, Na^+ concentration was computed by charge balance, where

$$[Na^+]_{calc} = \Sigma_{anion} - \Sigma_{cation}. \quad (47)$$

Sodium concentration determined by charge balance and by IC is tabulated in each of the site chapters, but only sodium concentration calculated by charge balance is plotted in the figures.

The minor elements (B, Ba, Fe, Li, Mn, Si, and Sr) were analyzed by ICP-AES (Horiba Jobin Yvon Ultima2). The interstitial water sample aliquot was diluted by a factor of 20 (0.5 mL sample added to 9.5 mL of 1% high-purity nitric acid solution spiked with 10 ppm yttrium). Because of the high concentration of matrix salts in interstitial water samples at a 1:20 dilution, matrix matching of the calibration standards is necessary to achieve accurate results by ICP-AES. A matrix solution that approximated sea-

water major ion concentrations was prepared by dissolving the following salts in 1 L of Milli-Q water acidified with 4 mL of optima-grade 6N HCl: 27 g NaCl, 3.8 g $MgCl_2$, 1.0 g $CaCO_3$, and 0.75 g KCl. Sulfate was not added to the matrix-matching solution because we expected the interstitial water sulfate concentration to decrease rapidly in the upper 20 m CSF, based on prior drilling results on this margin (Shipboard Scientific Party, 2001; Tobin et al., 2009, Underwood et al. 2009). Because the matrix solution was not a true blank, the procedural blank used was a dilution of 1% nitric acid solution in the yttrium solution, and only the slope of the calibration curve was used for quantification. A stock standard solution was prepared from ultrapure primary standards (SPC Science PlasmaCAL) in 1% nitric acid solution. The stock solution was then diluted in the same 1% ultrapure nitric acid solution to concentrations of 50%, 25%, 10%, 5%, and 1%. A 1.25 mL aliquot of each stock solution was added to 8.75 mL of matrix solution to produce a series of standards that could be diluted using the same method as the samples for consistency. The final matrix-matched 100% standard solution contained the following concentrations: B = 3000 µM, Li = 400 µM, Si = 1000 µM, Mn = 50 µM, Fe = 50 µM, Sr = 400 µM, and Ba = 200 µM. A standard prepared in the 10% matrix-matching solution was repeatedly analyzed to calculate the precision of the method. The average precision of the minor element analyses were B < 6%, Ba < 6%, Fe < 9%, Mn < 10%, Li < 7%, Si < 7%, and Sr < 7.

Vanadium, copper, zinc, molybdenum, rubidium, cesium, lead, and uranium were analyzed by ICP-MS (Agilent 7500ce ICP-MS) equipped with an octopole reaction system to reduce polyatomic and double-charge interferences. A 100 µL aliquot of 500 parts per billion (ppb) indium internal standard was added to the empty analysis vials before dilution. Sample aliquots were then diluted with 1% nitric acid solution to 10% in these vials (500 µL sample, 500 µL internal standard, and 4.0 mL of 0.15M HNO_3 solution) based on previous determination of the detection limits and the concentrations of the elements of interest. A primary standard solution that matched the maximum range of predicted concentrations was made based on published results of deep-sea interstitial water compositions in a variety of settings. The composition of the standard is as follows: V = 20 ppb; Cu, Mo, Pb, and U = 40 ppb; Zn = 140 ppb; Rb = 500 ppb; and Cs = 5 ppb. This primary standard was diluted in 1% nitric acid solution to relative concentrations of 50%, 25%, 10%, 5%, and 1%. The standards were diluted with the addition of 500 µL of a 560 mM NaCl solution, 500 µL of an internal standard, and 3.5 mL of 0.15M HNO_3 solution to account for matrix suppression of the plasma ionization efficiency. The 25% standard was diluted accordingly and analyzed every eight samples throughout every analysis series for precision and in order to compare the results from different analysis dates. Blanks were also analyzed every eight samples, and detection limits were determined as three times the standard deviation of a blank solution prepared with 500 µL internal standard and 4.5 mL of 0.15M HNO_3 solution. The average precision of multiple determinations of the 25% ICP-MS standard was V < 3.3%, Cu < 13.4%, Zn < 3.0%, Mo < 2.9%, Rb < 1.5%, Cs < 1.2%, Pb < 6.9%, and U < 17.7.

Organic geochemistry

The shipboard organic geochemistry program during Expedition 333 includes analyses of volatile hydrocarbon contents (C1–C4), elemental analyses of total carbon, nitrogen, and sulfur, as well as measurement of inorganic carbon content in sediments. The type and maturity of organic matter was characterized using Rock-Eval pyrolysis.

Hydrocarbon gas

For safety monitoring, concentrations and distributions of light hydrocarbon gases (C1–C4) were measured for each core following standard headspace sampling protocols. A 5 cm^3 sediment sample was collected with a cut-off plastic syringe from the freshly exposed end of the first section that was cut open in each core. When the sediments were too lithified, a cork borer was used for sampling. The sample was extruded into a 20 mL glass vial, immediately sealed with a PTFE coated septum, and then placed in a headspace sampler (Agilent Technologies G1888 network headspace sampler). The sample was heated at 70°C for 30 min before headspace gas was automatically injected into an Agilent 6890N gas chromatograph (GC) equipped with a packed column (GL HayeSep R) and flame ionization detector (FID). The carrier gas was helium at a constant flow rate of 32.8 mL/min. In the temperature program of the GC, the initial temperature of 100°C was held for 5.5 min before the temperature was ramped up at a rate of 5°C/min to 140°C and held isothermal for 4 min. Chromatographic response of the GC was calibrated against five different standards with variable quantities of low molecular weight hydrocarbons and checked on a daily basis.

Total carbon, nitrogen, and sulfur contents

Sediments for bulk geochemistry analyses were mostly taken from cluster samples, though some

samples were collected from working cores according to the requests of shipboard sedimentologists and organic geochemists. Sediments were freeze-dried and then ground using a planetary mill (Fristch). Total carbon (TC), total nitrogen (TN), and total sulfur (TS) contents were determined using a Thermo Finnigan Flash EA 1112 elemental analyzer. Calibration was based on the synthetic standard sulfanilamide, which contains 41.81 wt% C, 16.27 wt% N, and 18.62 wt% S.

About 40 mg of sediment was weighed and placed in a tin container for carbon and nitrogen analyses. For sulfur analysis, approximately 20 mg of sediment was weighed and put in a tin container with the V_2O_5 catalyst that was slightly >20 mg. Sediment samples were combusted in a stream of oxygen at 900°C for TC and TN and at 1000°C for TS. Nitrogen oxides were then reduced to N_2, and the mixture of CO_2, N_2, and SO_2 was separated by gas chromatography and detected by a thermal conductivity detector (TCD). The standard deviation of TC, TN, and TS concentrations determined from triplicate measurements of selected samples was within 0.01 wt%. Accuracy was confirmed using soil NCS reference material and a GSJ reference sample, with the measured value within 0.05, 0.04, and 0.1 wt% of the certified values for TC, TN, and TS, respectively.

Inorganic and organic carbon contents

In the same set of samples that was used for elemental analyses, inorganic carbon concentration was determined using a Coulometrics 5012 CO_2 coulometer. About 15–25 mg of freeze-dried ground sediment was weighed and reacted with 2M HCl. The amounts of liberated CO_2 were determined by trapping the CO_2 with ethanolamine and titrating coulometrically the hydroxyethylcarbamic acid that is formed. The weight percentage of calcium carbonate was calculated from the inorganic carbon content, assuming that all the measured CO_2 was derived from dissolution of calcium carbonate, by the following equation:

$$\mathrm{CaCO_3\ (wt\%)} = 8.333 \times \text{inorganic carbon (wt\%)}. \quad (48)$$

No correction was made for the presence of other carbonate minerals. National Institute of Standards and Technology–Standard Reference Material 88b was used to confirm accuracy, which was ±0.2 wt% from the certified value of inorganic carbon content (12.65 wt%). The standard deviation of inorganic carbon measurements was <0.02 wt%, based on triplicate analyses of selected samples. Total organic carbon (TOC) contents were calculated by subtracting inorganic carbon from the TC contents determined in elemental analyses.

Rock-Eval pyrolysis

Rock-Eval pyrolysis was used to characterize the type and maturity of the sedimentary organic matter. In principle, Rock-Eval pyrolysis consists of sequentially heating a sample in an inert atmosphere (nitrogen gas) within a pyrolysis oven. It allows us to quantitatively and selectively determine both the quantity of free hydrocarbons present in samples (S1) and the amounts of hydrocarbons (S2) and oxygen-containing compounds (S3) that are volatilized during thermal cracking of unextractable organic matter (kerogen).

During Expedition 333, Rock-Eval pyrolysis was performed using a Rock-Eval 6 analyzer (Vinci Technologies). S3 was not measured because the infrared cell was not functioning properly. S1, S2, and T_{max} were measured; hydrogen index (HI) and production index (PI) were calculated. S1 and S2 are expressed in milligrams of hydrocarbons per gram of sediment. S2 is an indicator of the quantity of hydrocarbons that the sediment can potentially produce should burial and maturation continue. T_{max} is the temperature at which the maximum release of hydrocarbons occurs from cracking of kerogen during pyrolysis. T_{max} is an indicator of organic matter maturity. HI (HI = [100 × S2]/TOC; in milligrams of hydrocarbon per gram of TOC) was calculated using TOC values yielded from the elemental analyzer. HI correlates with the ratio of H to C, which is higher for lipid- and protein-rich organic matter derived from marine algae than that from terrestrial plants. PI (PI = S1/[S1 + S2]) can indicate the evolution level of organic matter.

Rock-Eval analysis was conducted on samples that were selected according to their TOC and hydrocarbon gas contents. About 60–80 mg of sediment samples were obtained from the same freeze-dried and homogenized bulk samples that had been used for elemental analyses. The pyrolysis was kept at 300°C for 3 min, and then volatilized free hydrocarbons were measured by FID as the S1 peak. Subsequently, the temperature was raised from 300° to 550°C at 25°C/min. The hydrocarbons released from this thermal cracking were detected as the S2 peak by FID. The temperature of maximum detection of S2 was recorded as T_{max}. The values of all parameters were calibrated against IFPI 60000 reference materials (Vinci Technologies).

Igneous petrology

Core curation and sampling for shipboard measurements

To preserve important features and structures, all cores were passed through X-ray CT scan, and examined before being cut with a diamond-impregnated saw. Each piece was numbered sequentially from the top of the core section and labeled on the outside surface. Broken pieces that could be fit together were assigned the same number and were lettered consecutively (e.g., 1A, 1B, 1C, etc.). Rarely, composite pieces may have occupied more than one section. Plastic spacers were placed between pieces with different numbers.

The presence of a spacer may represent a substantial interval of no recovery. If it was evident that an individual piece had not rotated about a horizontal axis during drilling, an arrow pointing to the top of the section was added.

Nondestructive physical property measurements by multisensor core logger (MSCL) were made on the core before it was split (see **"Physical properties"**). Pieces were split with a diamond-impregnated saw in such a way that important compositional and structural features were preserved in both the archive and working halves. After splitting, digital images of the core were taken before description. The archive half was described on the VCD form for igneous characteristics, alteration, and structure. The working half was sampled for shipboard physical property measurements (see **"Physical properties"**), thin sections, and XRD. No samples were taken onboard for shore-based studies.

Visual core descriptions and barrel sheets for igneous rocks

We used general description VCD forms (Fig. **F17**) to document each section of the igneous rock cores. Symbols used on the VCDs are given in Figure **F18.** On the VCDs, the following are displayed from left to right:

- A scale from 0 to 150 cm,
- Piece number,
- Photograph of the archive half of the core,
- Piece orientation,
- Locations of samples selected for shipboard studies,
- Boundaries and number of lithologic units,
- Structures,
- Phenocrysts, and
- Alteration intensity.

Copies of VCDs are available from IODP upon request.

Vertically oriented pieces are indicated on the form by an upward-pointing arrow to the right of the appropriate piece. Locations of samples selected for shipboard studies are indicated in the Shipboard Studies column, using the following notation: XRD = X-ray diffraction analysis, XRF = X-ray fluorescence, TSB = petrographic thin section, PP = physical property analysis, or PMAG = paleomagnetic analysis. The Lithologic unit column displays the locations of boundaries between units and subunits and the unit designator (consecutive downhole subunits are designated by letters after the unit number; e.g., I, IIA, IIB, etc.). The Structure column displays graphical representations of structural types from the key in Figure **F18.**

During Expedition 333, we defined igneous rocks with glassy to fine-grained (average groundmass grain size = <1 mm) characteristics as volcanic rocks and the root term "basalt" was used. Basalt designates all igneous rocks of basaltic composition in the size range glassy to fine grained.

VCDs of volcanic rocks contain a text description of each unit in each section of core that includes:

- Summary description of unit as it appears in the section (e.g., pillow basalt or sheet flow);
- Rock name; and
- Additional comments, including phenocryst mineral abundance and size; groundmass grain size and texture, vesicle abundance, nature of alteration, description of structures in the rock, and any other additional comments.

In cryptocrystalline to microcrystalline rocks, there is a clear distinction between phenocrysts and groundmass crystals. These were described based on the identification of phenocrysts in hand sample following the criteria listed below.

Aphyric (<1% phenocrysts),
Sparsely phyric (1%–5% phenocrysts),
Moderately phyric (5%–10% phenocrysts), and
Highly phyric (>10% phenocrysts).

Rock names were further classified by types of phenocrysts present (e.g., sparsely plagioclase-olivine phyric, in which the amount of olivine exceeds the amount of plagioclase). An estimate of the percentage of vesicles and their average size was included in the VCDs. Vesicularity is described according to the abundance, size, and shape (sphericity and angularity) of the vesicles. The subdivision was made according to the following.

Nonvesicular (<1% vesicles),
Sparsely vesicular (1%–5% vesicles),

Moderately vesicular (5%–20% vesicles), and
Highly vesicular (>20% vesicles).

Pillow lavas were identified by curved chilled margins oblique to the vertical axis of the core or, when these margins were absent, curved fractures, and microcrystalline or cryptocrystalline grain size. Sheet flows were defined as thick intervals with the same rock type and grain size that increased toward the center of the flows. The most common types of contacts are those with chilled margins.

Thin section description of igneous rocks

During Expedition 333, five thin sections from the core intervals noted on the VCD forms were examined to complement and refine the hand specimen observations.

In general, the same terminology was used for thin section descriptions as for the VCDs. The percentages of individual phenocryst, groundmass, and alteration phases were estimated visually, and textural descriptions are reported in table format. The textural terms used are defined by MacKenzie et al. (1982).

Igneous units

The first level of core description is the definition of unit boundaries on the basis of the presence of contacts, chilled margins, changes in primary mineralogy, color, grain size, and structural or textural variations. Ideally, unit boundaries within volcanic rocks are meant to represent successive cooling units, but, when recovery is limited, unit boundaries may only represent changes in lithology.

References

Aguirre, E., and Pasini, G., 1985. The Pliocene–Pleistocene boundary. *Episodes,* 8:11–120.

ASTM International, 1990. Standard method for laboratory determination of water (moisture) content of soil and rock (Standard D2216–90). In *Annual Book of ASTM Standards for Soil and Rock* (Vol. 04.08): Philadelphia (Am. Soc. Testing Mater.). [revision of D2216-63, D2216-80]

Blum, P., 1997. Physical properties handbook: a guide to the shipboard measurement of physical properties of deep-sea cores. *ODP Tech. Note,* 26. **doi:10.2973/odp.tn.26.1997**

Bullard, E.C., 1939. Heat flow in South Africa. *Proc. R. Soc. London, Ser. A,* 173(955):474–502. **doi:10.1098/rspa.1939.0159**

Carlson, R.L., and Christensen, N.I., 1977. Velocity anisotropy and physical properties of deep-sea sediments from the western South Atlantic. *In* Supko, P.R., Perch-Nielsen, K., et al., *Init. Repts. DSDP,* 39: Washington, DC (U.S. Govt. Printing Office), 555–559. **doi:10.2973/dsdp.proc.39.124.1977**

Dunham, R.J., 1962. Classification of carbonate rocks according to depositional texture. *In* Ham, W.E. (Ed.), *Classification of Carbonate Rocks*. AAPG Mem., 1:108–121.

Embry, A.F., III, and Klovan, J.E., 1972. Absolute water depth limits of late Devonian paleoecological zones. *Geol. Rundsch.,* 61(2):672–686. **doi:10.1007/BF01896340**

Expedition 315 Scientists, 2009. Expedition 315 methods. *In* Kinoshita, M., Tobin, H., Ashi, J., Kimura, G., Lallemant, S., Screaton, E.J., Curewitz, D., Masago, H., Moe, K.T., and the Expedition 314/315/316 Scientists, *Proc. IODP,* 314/315/316: Washington, DC (Integrated Ocean Drilling Program Management International, Inc.). **doi:10.2204/iodp.proc.314315316.123.2009**

Expedition 316 Scientists, 2009. Expedition 316 methods. *In* Kinoshita, M., Tobin, H., Ashi, J., Kimura, G., Lallemant, S., Screaton, E.J., Curewitz, D., Masago, H., Moe, K.T., and the Expedition 314/315/316 Scientists, *Proc. IODP,* 314/315/316: Washington, DC (Integrated Ocean Drilling Program Management International, Inc.). **doi:10.2204/iodp.proc.314315316.132.2009**

Expedition 319 Scientists, 2010. Methods. *In* Saffer, D., McNeill, L., Byrne, T., Araki, E., Toczko, S., Eguchi, N., Takahashi, K., and the Expedition 319 Scientists, *Proc. IODP,* 319: Tokyo (Integrated Ocean Drilling Program Management International, Inc.). **doi:10.2204/iodp.proc.319.102.2010**

Expedition 322 Scientists, 2010. Methods. *In* Saito, S., Underwood, M.B., Kubo, Y., and the Expedition 322 Scientists, *Proc. IODP,* 322: Tokyo (Integrated Ocean Drilling Program Management International, Inc.). **doi:10.2204/iodp.proc.322.102.2010**

Expedition 333 Scientists, 2012a. Site C0011. *In* Henry, P., Kanamatsu, T., Moe, K., and the Expedition 333 Scientists, *Proc. IODP,* 333: Tokyo (Integrated Ocean Drilling Program Management International, Inc.). **doi:10.2204/iodp.proc.333.104.2012**

Expedition 333 Scientists, 2012b. Site C0012. *In* Henry, P., Kanamatsu, T., Moe, K., and the Expedition 333 Scientists, *Proc. IODP,* 333: Tokyo (Integrated Ocean Drilling Program Management International, Inc.). **doi:10.2204/iodp.proc.333.105.2012**

Expedition 333 Scientists, 2012c. Site C0018. *In* Henry, P., Kanamatsu, T., Moe, K., and the Expedition 333 Scientists, *Proc. IODP,* 333: Tokyo (Integrated Ocean Drilling Program Management International, Inc.). **doi:10.2204/iodp.proc.333.103.2012**

Fisher, A.T., and Underwood, M.B., 1995. Calibration of an X-ray diffraction method to determine relative mineral abundances in bulk powders using matrix singular value decomposition: a test from the Barbados accretionary complex. *In* Shipley, T.H., Ogawa, Y., Blum, P., et al., *Proc. ODP, Init. Repts.,* 156: College Station, TX (Ocean Drilling Program), 29–37. **doi:10.2973/odp.proc.ir.156.103.1995**

Fisher, R.V., and Schmincke, H.-U., 1984. *Pyroclastic Rocks:* New York (Springer-Verlag).

Fuller, M., 1969. Magnetic orientation of borehole cores. *Geophysics,* 34(5):772–774. **doi:10.1190/1.1440047**

GE Healthcare, 2006. *LightSpeed Series Learning and Reference Guide-Multi Slice CT:* Waukesha, Wisconsin (GE Healthcare), 936.

Gieskes, J.M., Gamo, T., and Brumsack, H., 1991. Chemical methods for interstitial water analysis aboard *JOIDES Resolution*. *ODP Tech. Note,* 15. **doi:10.2973/odp.tn.15.1991**

Heard, T.G., Pickering, K.T., and Robinson, S.A., 2008. Milankovitch forcing of bioturbation intensity in deep-marine thin-bedded siliciclastic turbidites. *Earth Planet. Sci. Lett.,* 272(1–2):130–138. **doi:10.1016/j.epsl.2008.04.025**

Hilgen, F.J., 2008. Recent progress in the standardization and calibration of the Cenozoic time scale. *Newsl. Stratigr.,* 43(1):15–22. **doi:10.1127/0078-0421/2008/0043-0015**

Kimura, G., Silver, E.A., Blum, P., et al., 1997. *Proc. ODP, Init. Repts.,* 170: College Station, TX (Ocean Drilling Program). **doi:10.2973/odp.proc.ir.170.1997**

Kirschvink, J.L., 1980. The least-squares line and plane and the analysis of palaeomagnetic data. *Geophys. J. R. Astron. Soc.,* 62(3):699–718. **doi:10.1111/j.1365-246X.1980.tb02601.x**

Kodama, K.P., 1984. Palaeomagnetism of granitic intrusives from the Precambrian basement under eastern Kansas: orienting drill cores using secondary magnetization components. *Geophys. J. R. Astron. Soc.,* 76(2):273–287. **doi:10.1111/j.1365-246X.1984.tb05045.x**

Lourens, L., Hilgen, F., Shackleton, N.J., Laskar, J., and Wilson, D., 2004. The Neogene period. *In* Gradstein, F.M., Ogg, J.G., and Smith, A. (Eds.), *A Geologic Time Scale 2004:* Cambridge (Cambridge Univ. Press), 409–440.

MacKenzie, W.S., Donaldson, C.H., and Guilford, C., 1982. *Atlas of Igneous Rocks and Their Textures:* Essex, England (Longman Group UK Limited).

Manheim, F.T., 1966. A hydraulic squeezer for obtaining interstitial waters from consolidated and unconsolidated sediments. *Geol. Surv. Prof. Pap. (U.S.),* 550-C:256–261.

Martini, E., 1971. Standard Tertiary and Quaternary calcareous nannoplankton zonation. *Proc. Int. Conf. Planktonic Microfossils,* 2:739–785.

Mazzullo, J., and Graham, A.G. (Eds.), 1988. Handbook for shipboard sedimentologists. *ODP Tech. Note,* 8. **doi:10.2973/odp.tn.8.1988**

Mazzullo, J.M., Meyer, A., and Kidd, R.B., 1988. New sediment classification scheme for the Ocean Drilling Program. *In* Mazzullo, J.M., and Graham, A.G. (Eds.), *Handbook for shipboard sedimentologists*. ODP Tech. Note, 8:45–67. **doi:10.2973/odp.tn.8.1988**

Mees, F., Swennen, R., Van Geet, M., and Jacobs, P., 2003. Applications of X-ray computed tomography in the geosciences. *Geol. Soc. Spec. Publ.,* 215(1):1–6. **doi:10.1144/GSL.SP.2003.215.01.01**

Mizutani, S., Saito, Y., and Kanmera, K. (Eds.), 1987. *Sedimentary Rocks in Japan:* Tokyo (Iwanami Shoten). (in Japanese)

Moore, G.F., Taira, A., Klaus, A., et al., 2001. *Proc. ODP, Init. Repts.,* 190: College Station, TX (Ocean Drilling Program). **doi:10.2973/odp.proc.ir.190.2001**

Nakano, T., Nakashima, Y., Nakamura, K., and Ikeda, S., 2000. Observation and analysis of internal structure of rock using X-ray CT. *Chishitsugaku Zasshi,* 106(5):363–378.

Okada, H., and Bukry, D., 1980. Supplementary modification and introduction of code numbers to the low-latitude coccolith biostratigraphic zonation (Bukry, 1973; 1975). *Mar. Micropaleontol.,* 5:321–325. **doi:10.1016/0377-8398(80)90016-X**

Perch-Nielsen, K., 1985. Cenozoic calcareous nannofossils. *In* Bolli, H.M., Saunders, J.B., and Perch-Nielsen, K. (Eds.), *Plankton Stratigraphy:* Cambridge (Cambridge Univ. Press), 427–554.

Raffi, I., Backman, J., Fornaciari, E., Pälike, H., Rio, D., Lourens, L., and Hilgen, F., 2006. A review of calcareous nannofossil astrobiochronology encompassing the past 25 million years. *Quat. Sci. Rev.,* 25(23–24):3113–3137. **doi:10.1016/j.quascirev.2006.07.007**

Rothwell, R.G., 1989. *Minerals and Mineraloids in Marine Sediments: An Optical Identification Guide:* London (Elsevier).

Sato, T., and Takayama, T., 1992. A stratigraphically significant new species, *Reticulofenestra asanoi* (calcareous nannofossil). *In* Ishizaki, K., and Saito, T. (Eds.), *Centenary of Japanese Micropaleontology:* Tokyo (Terra Sci. Publ.), 457–460. **http://www.terrapub.co.jp/e-library/cjm/pdf/0457.pdf**

Shepard, F.P., 1954. Nomenclature based on sand-silt-clay ratios. *J. Sediment. Petrol.,* 24(3):151–158. **http://jsedres.sepmonline.org/cgi/reprint/24/3/151.pdf**

Shibuya, H., Merrill, D.L., Hsu, V., and Leg 124 Shipboard Scientific Party, 1991. Paleogene counterclockwise rotation of the Celebes Sea—orientation of ODP cores utilizing the secondary magnetization. *In* Silver, E.A., Rangin, C., von Breymann, M.T., et al., *Proc. ODP, Sci. Results,* 124: College Station, TX (Ocean Drilling Program), 519–523. **doi:10.2973/odp.proc.sr.124.169.1991**

Shipboard Scientific Party, 2001. Site 1177. *In* Moore, G.F., Taira, A., Klaus, A., et al., *Proc. ODP, Init. Repts.,* 190: College Station, TX (Ocean Drilling Program), 1–91. **doi:10.2973/odp.proc.ir.190.108.2001**

Shipley, T.H., Ogawa, Y., Blum, P., et al., 1995. *Proc. ODP, Init. Repts.,* 156: College Station, TX (Ocean Drilling Program). **doi:10.2973/odp.proc.ir.156.1995**

Taira, A., Hill, I., Firth, J.V., et al., 1991. *Proc. ODP, Init. Repts.,* 131: College Station, TX (Ocean Drilling Program). **doi:10.2973/odp.proc.ir.131.1991**

Takayama, T., and Sato, T., 1987. Coccolith biostratigraphy of the North Atlantic Ocean, Deep Sea Drilling Project Leg 94. *In* Ruddiman, W.F., Kidd, R.B., Thomas, E., et al., *Init. Repts. DSDP,* 94: Washington, DC (U.S. Govt. Printing Office), 651–702. **doi:10.2973/dsdp.proc.94.113.1987**

Takayama, T., and Sato, T., 1993–1995. Coccolith biostratigraphy of the Pliocene/Pleistocene boundary stratotype. *Ann. Geol. Pays Hell.,* 36:143–150.

Tobin, H., Kinoshita, M., Ashi, J., Lallemant, S., Kimura, G., Screaton, E.J., Moe, K.T., Masago, H., Curewitz, D., and the Expedition 314/315/316 Scientists, 2009. NanTroSEIZE Stage 1 expeditions: introduction and synthesis of key results. *In* Kinoshita, M., Tobin, H., Ashi, J., Kimura, G., Lallemant, S., Screaton, E.J., Curewitz, D., Masago, H., Moe, K.T., and the Expedition 314/315/316 Scientists, *Proc. IODP,* 314/315/316: Washington, DC (Integrated Ocean Drilling Program Management International, Inc.). **doi:10.2204/iodp.proc.314315316.101.2009**

Underwood, M.B., Basu, N., Steurer, J., and Udas, S., 2003. Data report: normalization factors for semiquantitative X-ray diffraction analysis, with application to DSDP Site 297, Shikoku Basin. *In* Mikada, H., Moore, G.F., Taira, A., Becker, K., Moore, J.C., and Klaus, A. (Eds.), *Proc. ODP, Sci. Results,* 190/196: College Station, TX (Ocean Drilling Program), 1–28. **doi:10.2973/odp.proc.sr.190196.203.2003**

Underwood, M.B., Saito, S., Kubo, Y., and the Expedition 322 Scientists, 2009. NanTroSEIZE Stage 2: subduction inputs. *IODP Prel. Rept.,* 322. **doi:10.2204/iodp.pr.322.2009**

Vacquier, V., 1985. The measurement of thermal conductivity of solids with a transient linear heat source on the plane surface of a poorly conducting body. *Earth Planet. Sci. Lett.,* 74(2–3):275–279. **doi:10.1016/0012-821X(85)90027-5**

Von Herzen, R.P., and Maxwell, A.E., 1959. The measurement of thermal conductivity of deep-sea sediments by a needle-probe method. *J. Geophys. Res.,* 64(10):1557–1563. **doi:10.1029/JZ064i010p01557**

Young, J.R., 1998. Neogene. *In* Bown, P.R. (Ed.), *Calcareous Nannofossil Biostratigraphy:* Dordrecht, The Netherlands (Kluwer Academic Publ.), 225–265.

Publication: 18 May 2012
MS 333-102

Figure F1. IODP conventions for naming sites, holes, cores, and samples. mbsl = meters below sea level, mbsf = meters below seafloor.

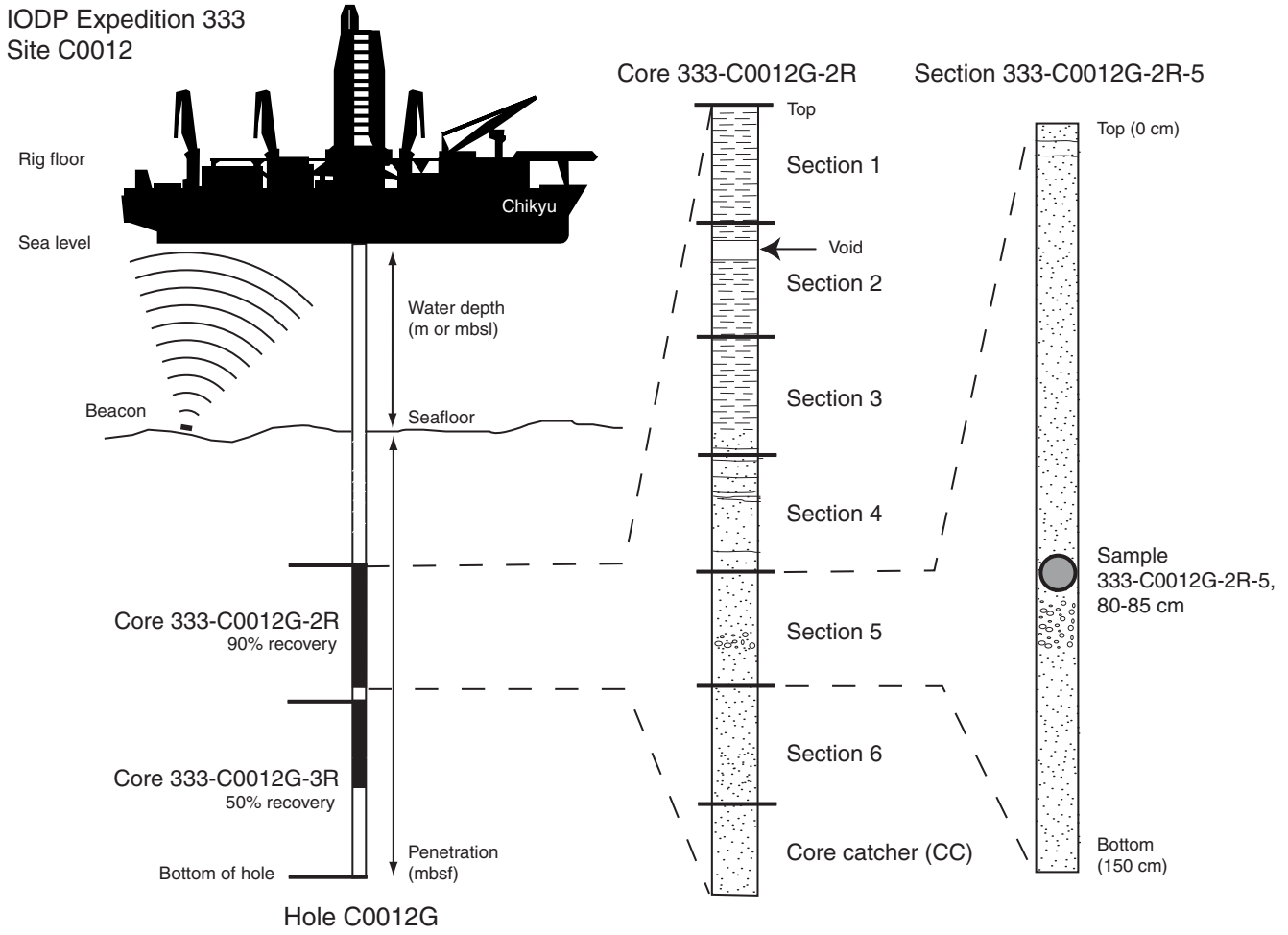

Figure F2. Overview of standard core flow from rig floor, through core cutting, core processing, description, sampling, and storage area. X-CT = X-ray computed tomography, MSCL-W = whole-round multisensor core logger, GRA = gamma ray attenuation, MS = magnetic susceptibility, NGR = natural gamma ray, RMS = routine microbiology sampling, VCD = visual core description, MSCL-C = contact core logger, MSCL-I = imaging core logger, MAD = moisture and density, XRD = X-ray diffraction, XRF = X-ray fluorescence, PWV = *P*-wave velocity, ER = electrical resistivity, GC = gas chromatograph, FID = flame ionization detector, UV = ultraviolet, ICP-AES = inductively coupled plasma–atomic emission spectroscopy, ICP-MS = inductively coupled plasma–mass spectrometry, CHNS = carbon-hydrogen-nitrogen-sulfur analyzer, XRF-CL = X-ray fluorescence–core logger. (Figure shown on next page.)

Figure F2 (continued). (Caption shown on previous page.)

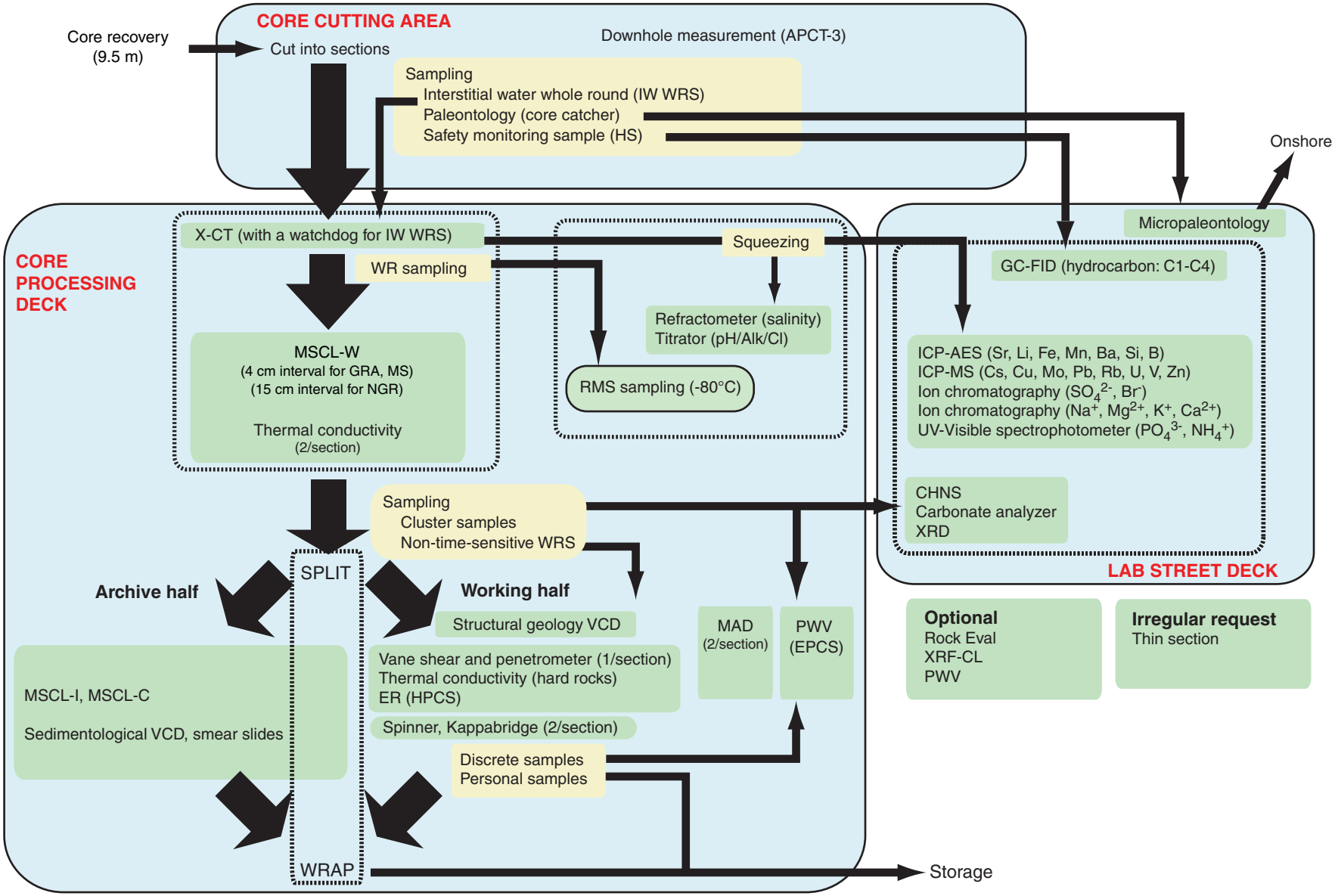

Figure F3. Graphic patterns for the lithologies encountered during Expedition 333.

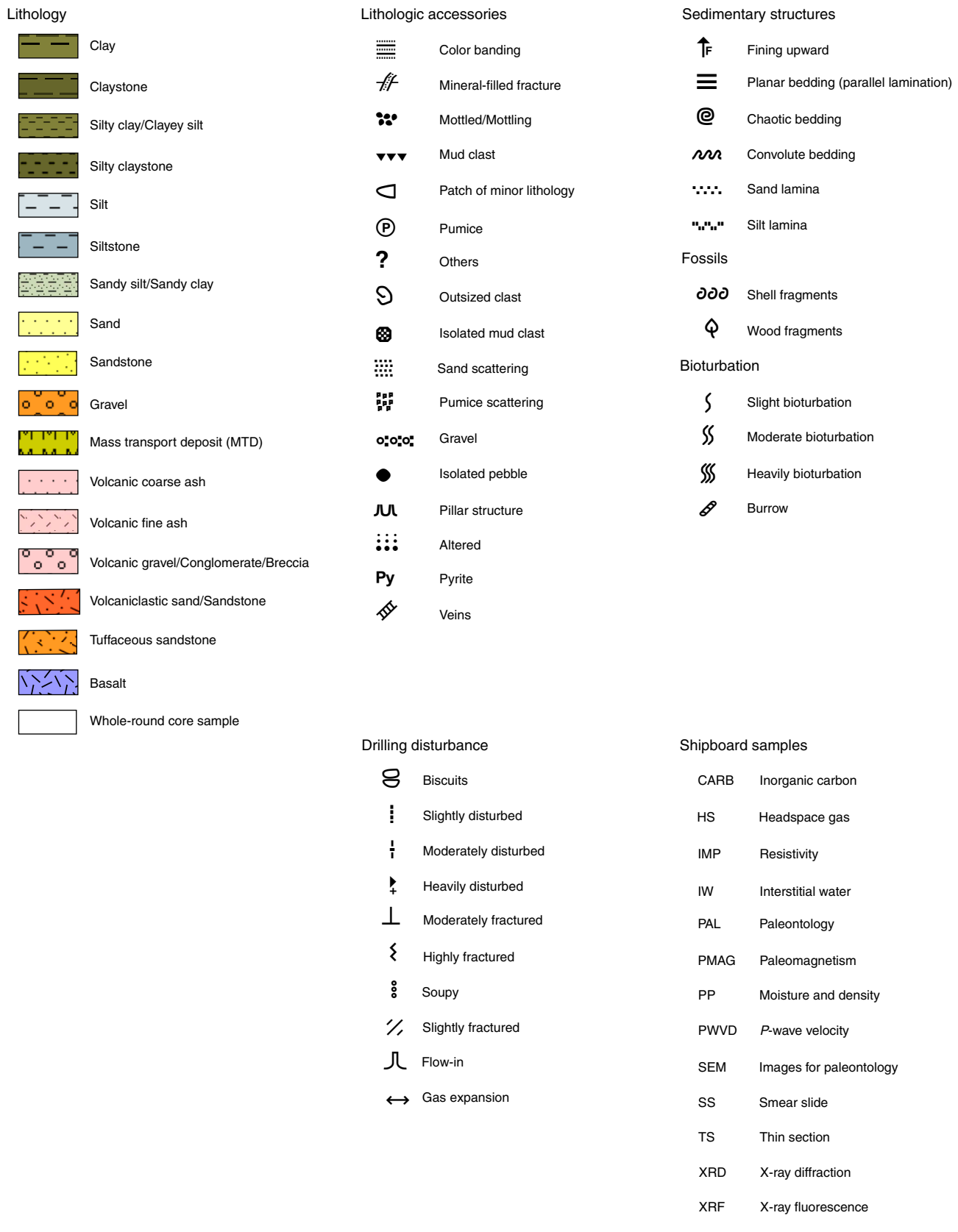

Figure F4. Smear slide data interpreted during Expedition 333. Indicated in the table are the core and section numbers, together with the relative depth from which smear samples were taken.

Exp: 333
Site: 0018A

[Legend] D: dominant (>50%), A: abundant (>20-50%), C: common (>5-20%), P: present (>1-5%), R: rare (>0.1-1%), T: trace (<0.1%)

				Texture			Siliclastic Grain									Lithic Grains or Ash					Pelagic Grains							Other		Coments	
Hole-Core-Sec	Int. (cm)	Depth (msf)	Lithology	Sand	Silt	Clay	Quartz	Feldspar	Mica Group	Opaque Min.	Glauconite	Clay Min.	Zeolite	Heavy Min.	Calcite/Carbonate Min.	Sed. Lithic	Ign. Lithic	Meta. Lithic	Volcanic Lithic	Vol. Glass	Nannofossils	Foraminifers	Diatoms	Radiolarians	Silicoflagellates	Sponge spicules	Clay Mins.	Zeolithe	[Legend] Ap: Apatite, Bt: Biotite, Chl: Chlorite, Cpx: Clinopyroxene, Cum: Cumingtonite, Hbl: Hornblende, Ogn: Organic materials, Opx: Orthopyroxene, Pyr: Pyrite, Zr: Zircon	
1H-1-36			Silty clay	0	40	60	R					A		R						P	A	P	C	R	P	C				
1H-3-36			Silty clay	0	30	70	R	R				A		R						P	A	R	C	R	P	C			Ogn	
1H-3-115			Silty clay	0	30	70	R	R				A		R						C	A	R	C	R	P	C				
1H-4-66			**Silty clay**	**5**	**35**	**60**	**T**					**A**		**P**						**P**	**A**	**P**	**C**	R	R	C			**fish materials?**	**Interval 1**
1H-4-88			**Silty clay**	**5**	**35**	**60**	**R**					**A**		**R**						**P**	**C**	P	C	P	R	C				
1H-4-135			Sandy silt	5	40	55	R	T				A		R						C	C	C	P	R		P			Ogn	
1H-5-30			Silty clay	1	30	69	R					A		R						P	A	P	C	R	T	C				
1H-7-112			Silty clay	1	20	79	P	R				A		R						P	A	R	C	T	T	C				
2H-1-90			Silty clay	0	20	80	R					D		R						P	A	R	C	T	R	C				
2H-3-98			Silty clay	1	30	69	P	R	R			A		R						P	C	C	C	R	T	P			colored vol. glasses	
2H-4-68			Silty clay with volcanic ash	5	30	65	P	R	R			A		P						P	A	C	C	T	T	C				
2H-5-38			Silty clay with volcanic ash	1	20	79	R		R			D		T						P	A	C	C	R	T	C				
2H-7-87.5			Silty clay	3	20	77	P		R			A		T						P	A	R	C	T		P			colored vol. glasses	
2H-8-117			Silty clay	2	20	78	P	R				C		T						R	A	R	P		T	P				
2H-9-35			Silty clay	10	50	40		R				C		T						P	A	R	C		T	P				
2H-11-108			Silty clay	2	30	68		R				C		T					R	C	A		C	R	T	P				
3H-1-38			Silty clay	1	10	89	R	R				A		R						R	A	R	C			P				
3H-2-89			Clay	1	3	96	P	T				A		T						R	A		C		T	T				
3H-2-133			Clay	1	3	96	R			R		A		T						T	A	T	P		T	T			Pyr, Blue minerals	
3H-4-33			Silty clay	7	25	68	T		T			C		T						T	A		C	P	P	P				
3H-6-57			Silty clay	1	30	69	P			R		C		T						C	A	T	C	T		P			Pyr	
3H-7-102			Silty clay	0	20	80	R	R				C		T						T	A	T	P		T	P				
3H-8-108			Volcanic ash	1	50	49	R					P								A	C	R	P			R				
3H-9-44			Silty clay	1	10	89	P		T			C								T	A	R	C			T			Brown colored vol. glasses	
4H-1-124			Silty clay	0	10	90	R					A									A	R	P			P				
4H-2-86			Silty clay	2	5	93	P	R		R		C		T							A	R	P		T	R				
4H-3-77			Volcanic ash	60	25	15	T	R		R		T		T						D	C		R						Brown colored vol. glasses	
4H-5-105			Silty clay	1	10	89	P	R				A		T						T	A		C		T	P				
4H-6-97			Silty clay	1	15	84	P	R				A		T						T	A	T	P	T		T				
4H-7-105			Silty clay	0	10	90	R	R		P		A									A		C			P				
4H-8-38			Silty clay with volcanic ash	5	20	75	R	R		R		A		R						C	A	P	P	R	R	P				
4H-cc-16			Silty clay	1	10	89	R	R	T	T		A		T						R	A	R	C	T	T	P				
5H-1-100			Silty clay	0	10	90	R	R	T	T		A		T						R	D	T	C	T	T	R				
5H-2-33.5			Silty clay with volcanic ash	5	20	75	R	T	T	T		A								C	A	C	C		T	R				

Figure F5. Classification of lithic components in siliciclastic sediment (neritic, pelagic, volcaniclastic and siliciclastic). Modified from Mazzullo and Graham (1988).

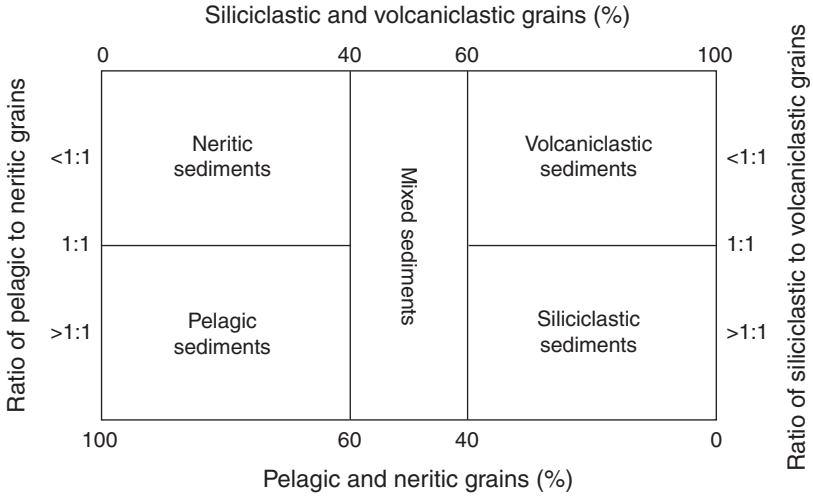

Figure F6. Log sheet used to record structural data and observations from working half of split core.

CHIKYU Operation

Structural Geology Observation Sheet

No.

Exp. : Site : Core : Observer : Summary:

Section No.	Structure ID	Top of Struct	Bottom of Struct	ave, depth	Core face app. Dip		2nd app. Dip		Striation on surface		Coherent interval (for P-mag)		P-mag pole		notes
					az.	dip	az.	dip	rake	from	top	bottom	az./trend	dip	

VCD_sheet_str100805

Figure F7. Modified protractor used to measure apparent dip, trend, plunge, and rake on planar and linear features in a split core.

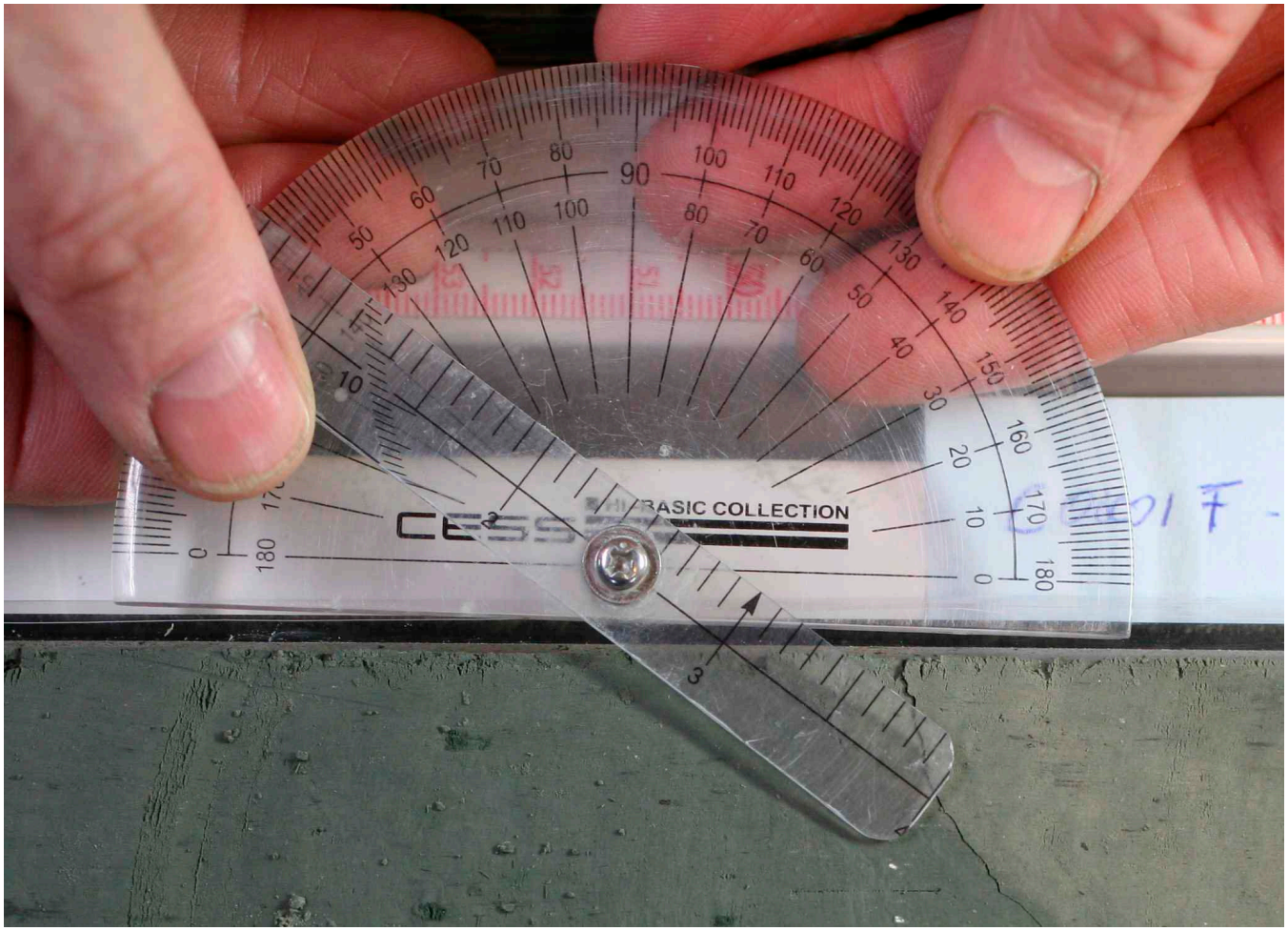

Figure F8. Core coordinate system with *x*-, *y*-, and *z*-axes used in orientation data calculations.

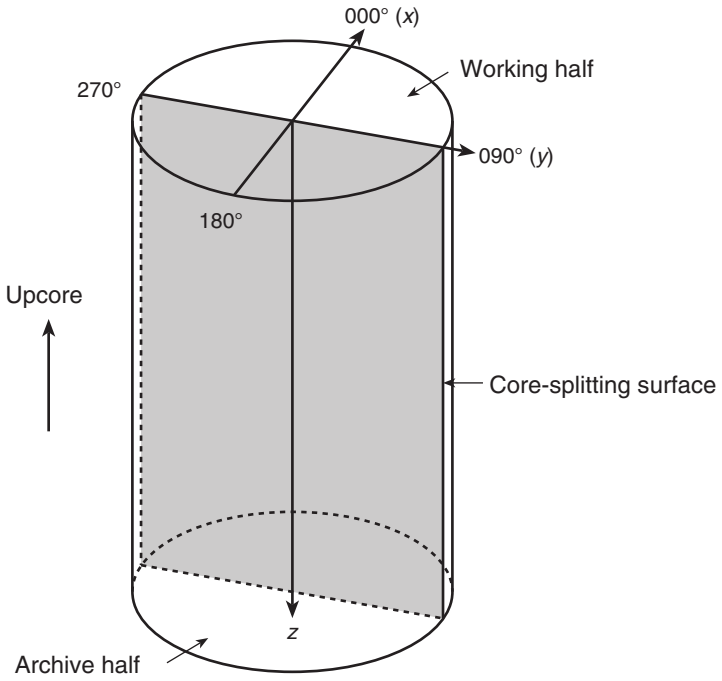

Figure F9. Spreadsheet used for recording and calculating orientation data.

C00018				structure ID	top of struct	bottom of struct	average depth	core face app. dip		2nd app. dip		striation on surface		plane-normal orientation					plane orientation (RHR)			fault			coherent interval (for P-mag)		P-mag pole		corrected orientation (RHR)			fault		notes
depth	hole	core	sect					az	dip	az	dip	rake	from	l	m	n	az	dip	dip dir	strike	dip	csf rake	str rake	slip sense	top	bottom	Dec	Inc	dip dir	strike	dip	str rake	slip sense	
1.86	A	1H	3	bedding	44.0	45.0	44.5	90	14	332	0			0.11	0.21	-0.86	62	-74	62	332	16				0	140	288.861	53.662	133	43	16			
29.52	A	4H	3	bedding	86.0	87.0	86.5	270	1	180	9			-0.16	-0.02	-0.99	186	-81	186	96	9				0	92	37.8078	54.335	148	58	9			
54.33	A	7H	1	dewatering structure?	14.0	21.0	17.5																											
64.30	A	7H	11	fault	135.0	137.0	136	90	38	59	0			-0.53	0.32	-0.41	149	-33	149	59	57				17	144	267.54	65.815	241	151	57			
64.27	A	8H	2	bedding	35.0	37.0	36	90	27	56	0			-0.38	0.25	-0.50	146	-48	146	56	42				0	98	10.1184	45.135	136	46	42			
65.97	A	8H	3	bedding	59.0	60.0	59.5	90	3	323	0			0.03	0.04	-0.80	53	-86	53	323	4				52	115	10.1184	45.135	43	313	4			
67.15	A	8H	4	disturbed layers	50.0	75.0	62.5																											
69.47	A	8H	8	fault	8.0	21.0	14.5	270	66	325	0			0.52	0.75	0.33	55	20	235	145	70			N	0	147	10.1184	45.135	225	135	70		N	offset = 8 mm
73.51	A	8H	10	fault	118.0	129.0	123.5	90	66	319	0			0.60	0.69	-0.31	49	-19	49	319	71				108	148	10.1184	45.135	39	309	71			
105.56	A	12H	7	fault	22.0	26.0	24	90	37	287	0			0.58	0.18	-0.23	17	-21	17	287	69			N	0	140	230.055	57.395	147	57	69		N	offset = 8.5mm
106.10	A	12H	7	bedding	77.0	78.0	77.5	90	1	0	0			0.00	0.02	-1.00	90	-89	90	0	1				0	140	230.055	57.395	220	130	1			
110.72	A	13H	4	fault	0.0	10.0	5	270	64	337	0			0.35	0.83	0.40	67	24	247	157	66				0	54	67.1364	43.259	180	90	66			syn-sedimentary
112.32	A	13H	5	bedding	23.0	24.0	23.5	270	2	62	0			-0.03	0.02	0.47	152	86	332	242	4				15	46	67.1364	43.259	265	175	4			
114.53	A	13H	9	fault	6.0	14.0	10	90	52	16	0			-0.22	0.76	-0.59	106	-37	106	16	53			T	0	89	67.1364	43.259	39	309	53		T	offset = 20 mm
117.65	A	13H	11	fault	35.0	48.0	41.5	270	62	20	0			-0.30	0.83	0.44	110	27	290	200	63			N	0	49	67.1364	43.259	223	133	63		N	offset = 28 mm
119.29	A	13H	13	fault	130.0	137.0	133.5	270	63	150	0			-0.45	-0.77	-0.39	240	-24	240	150	66				0	138	67.1364	43.259	173	83	66			
141.96	A	16H	10	fault	17.0	26.0	21.5	90	50	180	45	11	270	0.45	-0.54	0.45	310	33	130	40	57	66	77		0	76	350.371	-70.37	320	230	57	77	0	
143.09	A	16H	11	fault	54.0	60.0	57	90	40	312	0	30	90	0.48	0.43	-0.51	42	-39	42	312	51	125	95		12	122	350.371	-70.37	232	142	51	95	0	
141.09	A	16H	4	fault (not healed)	79.0	88.0	83.5	90	57	32	0	11	270	-0.44	0.71	-0.46	122	-29	122	32	61	73	84		0	149	350.371	-70.37	312	222	61	84	0	
141.57	A	16H	4	fault (not healed)	129.0	135.0	132	90	56	35	0			-0.48	0.68	-0.46	125	-29	125	35	61				0	149	350.371	-70.37	315	225	61			
142.91	A	16H	11	fault (not healed)	36.0	42.0	39	90	46	310	0	35	90	0.55	0.46	-0.45	40	-32	40	310	58	122	87	N	12	121	350.371	-70.37	230	140	58	87	N	
143.09	A	16H	11	fault (not healed)	54.0	60.0	57	90	40	312	0	30	90	0.48	0.43	-0.51	42	-39	42	312	51	125	95	N	12	121	350.371	-70.37	232	142	51	95	N	
145.38	A	17H	1	bedding	72.0	73.0	72.5	90	21	338	0			0.13	0.33	-0.87	68	-68	68	338	22				0	82	345.925	-68.26	262	172	22			
145.18	A	17H	1	shear zone	49.0	57.0	53	90	51	320	0			0.50	0.60	-0.48	50	-32	50	320	58				34	143	345.925	-68.26	244	154	58			
149.60	A	17H	4	shear zone	69.0	75.0	72	270	63	45	0			-0.63	0.63	0.32	135	20	315	225	70				0	141	345.925	-68.26	149	59	70			
151.54	A	17H	7	web structure	10.0	52.0	31																											
152.27	A	17H	7	shear zone	103.0	105.0	104	270	17	80	0			-0.29	0.05	0.17	170	30	350	260	60				0	143	345.925	-68.26	184	94	60			
152.51	A	17H	7	shear zone	123.0	133.0	128	90	66	308	0			0.72	0.56	-0.25	38	-15	38	308	75				0	143	345.925	-68.26	232	142	75			
												≤90	±1, 90 or 270 top->"1" bottom->"-1"														Red means uncertain data						

Figure F10. Calculation of plane orientation (shaded) from two apparent dips. Intersections of split core surface and section perpendicular to split core surface and parallel to core direction with plane of interest are shown. (α_1, β_1) and (α_2, β_2) = azimuths and dips of traces of the plane on two sections, v_1 and v_2 = unit vectors parallel to traces of the plane on two sections, v_n = unit vector normal to plane.

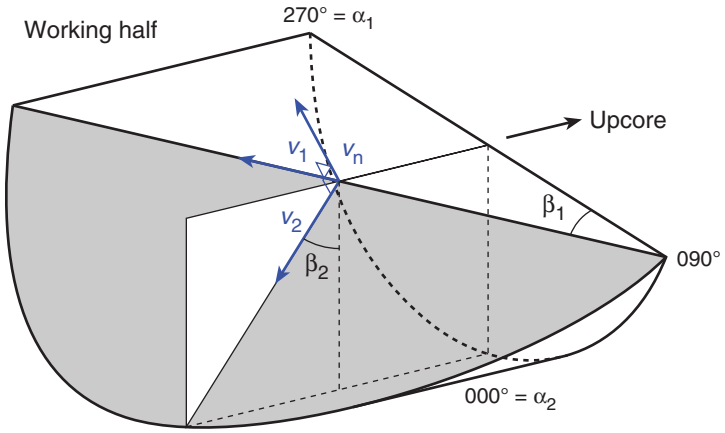

Figure F11. Dip direction (α_d), right-hand rule strike (α_s), and dip (β) of a plane deduced from its normal azimuth (α_n) and dip (β_n). **A.** $\beta_n < 0°$. **B.** $\beta_n \geq 0°$. v_n = unit vector normal to plane.

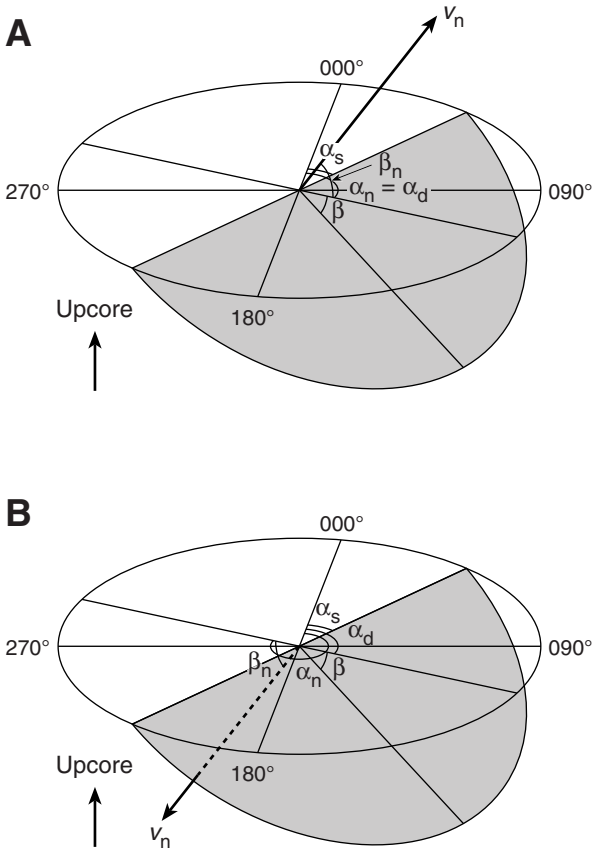

Figure F12. Apparent rake measurement of slickenlines on a fault surface from 270° direction of split core surface trace. ϕ_a = apparent rake, v_n = unit vector normal to fault plane, v_c = unit vector normal to split core surface, v_i = unit vector parallel to the intersection line between fault plane and split core surface.

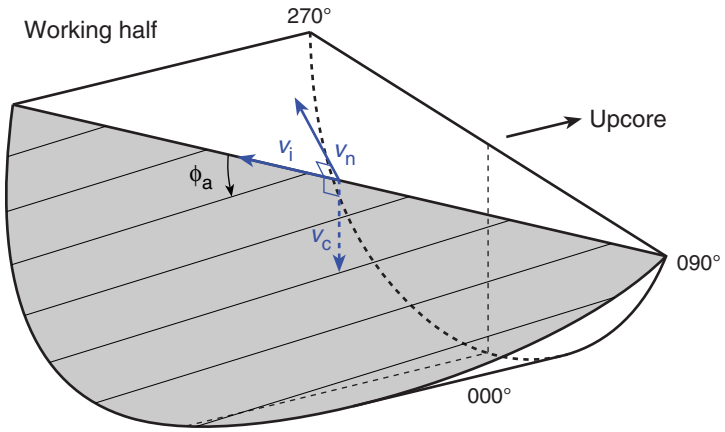

Figure F13. Rake of slickenlines (ϕ) deduced from the rake of intersection line between fault plane and split core surface (ϕ_i) and apparent rake measured (ϕ_a). **A.** ϕ_a from top or 090° direction where fault plane dips westward. **B.** ϕ_a from bottom or 090° direction where fault plane dips eastward. **C.** ϕ_a from top or 270° direction where fault plane dips eastward. **D.** ϕ_a from bottom or 270° direction where fault plane dips westward. α_s = right-hand rule strike of fault plane, v_n = unit vector normal to fault plane, v_c = unit vector normal to split core surface, v_i = unit vector parallel to intersection line between fault plane and split core surface. v_s = horizontal unit vector in the right-hand rule strike direction of fault plane.

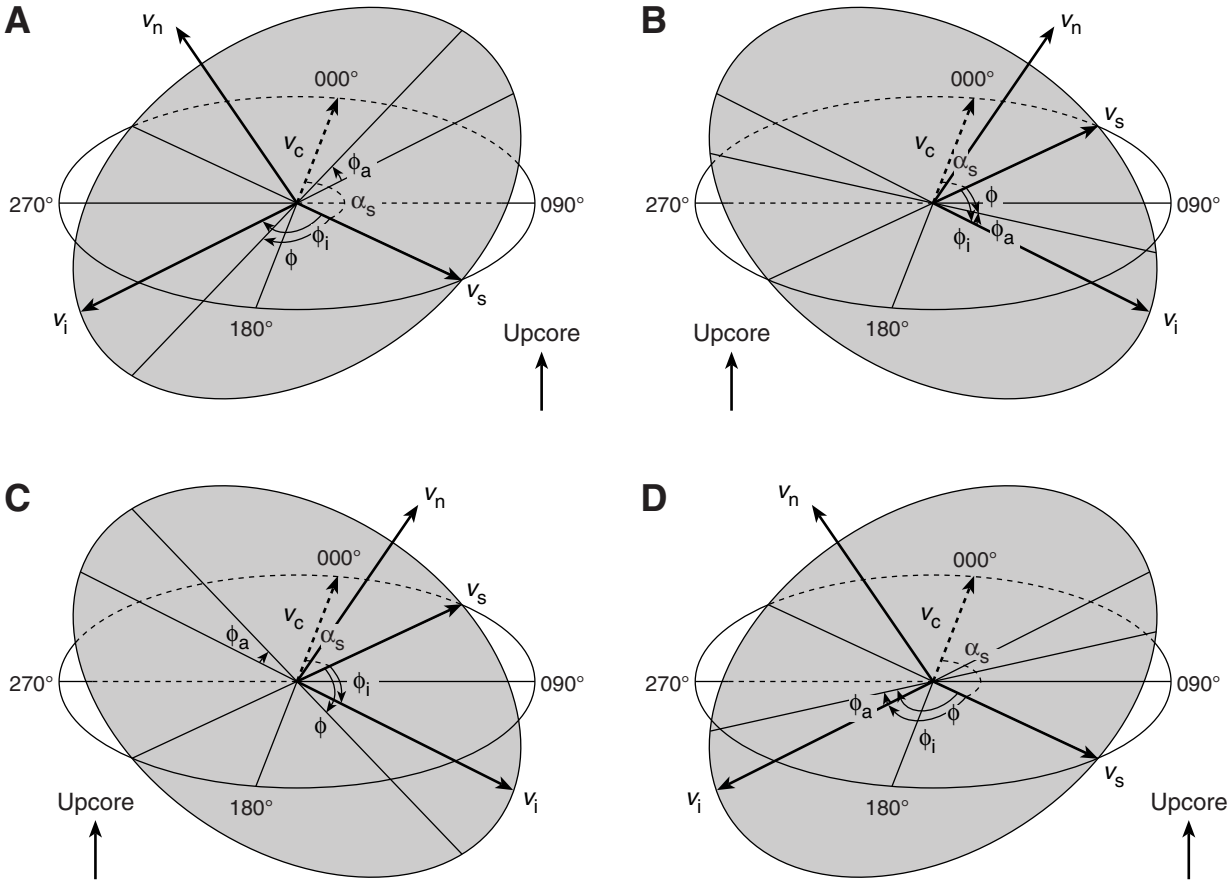

Figure F14. Azimuth correction based on paleomagnetic data. **A.** Paleomagnetic inclination $\beta_p \geq 0°$. **B.** Paleomagnetic inclination $\beta_p < 0°$. α_p = paleomagnetic declination, α_d and α_s = dip direction and right-hand rule strike of a plane.

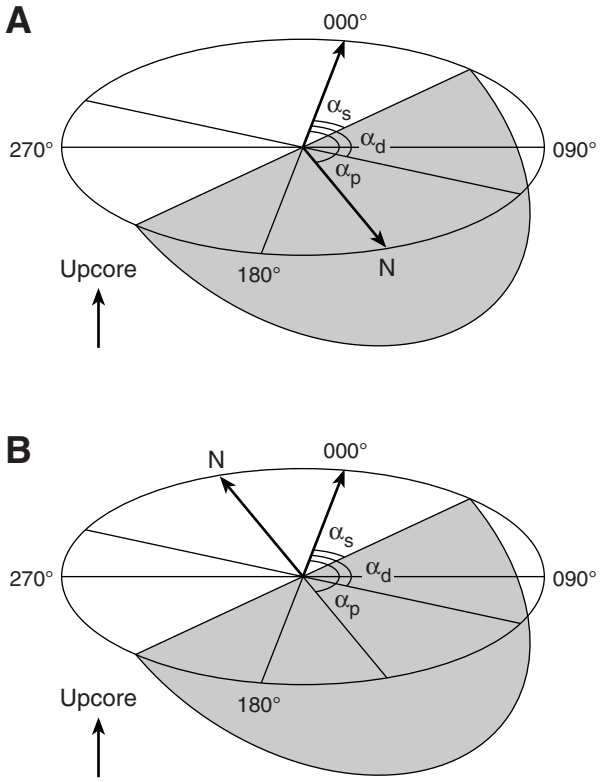

Figure F15. Correlation of geomagnetic polarity timescale (Lourens et al., 2004), biostratigraphic zonation, and biohorizons used during Expedition 333. FO = first occurrence, LO = last occurrence, LCO = last consistent occurrence, FCO = first consistent occurrence, PE = paracme end, PB = paracme beginning.

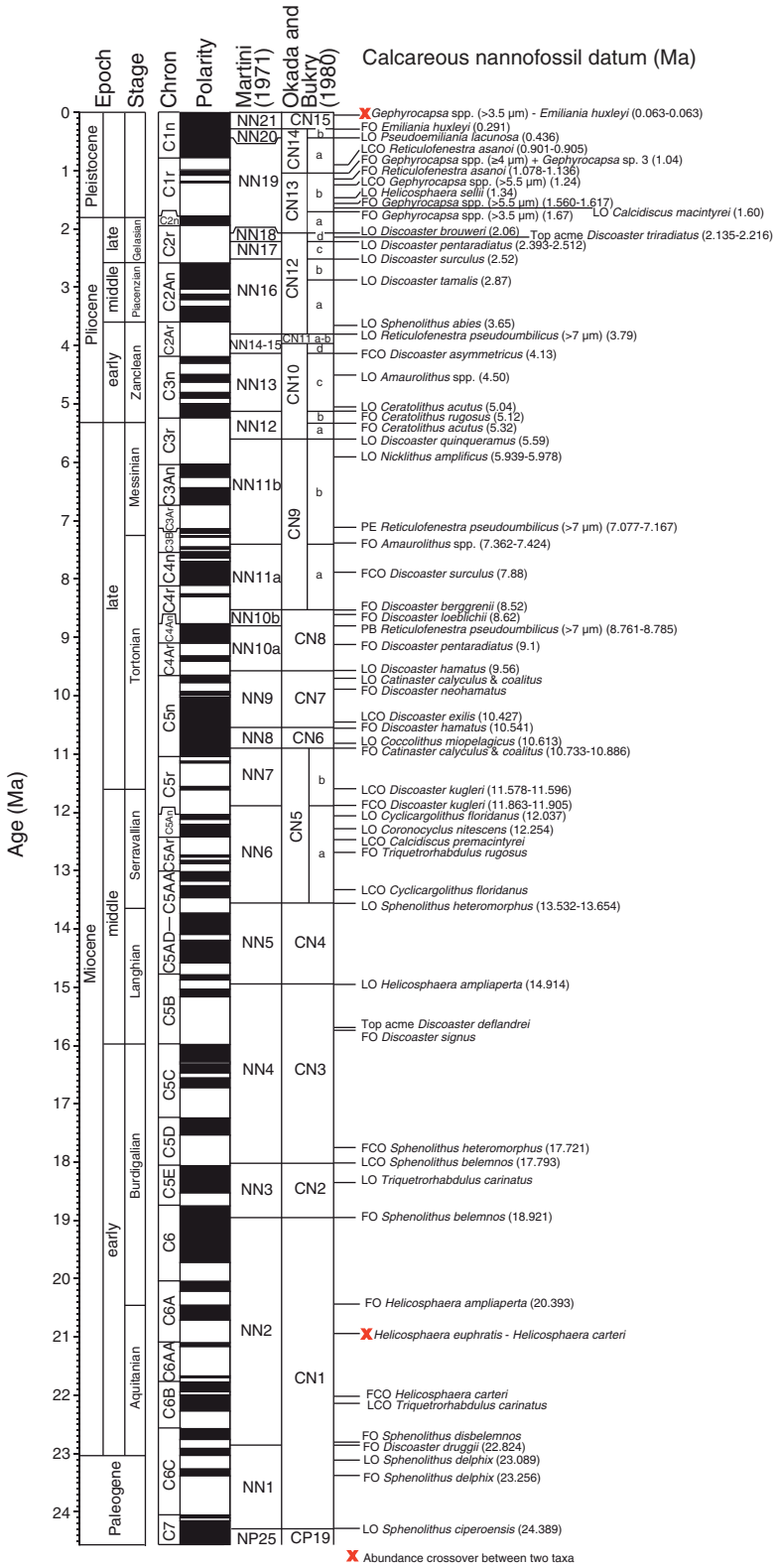

Figure F16. Orientation system of cores, discrete samples, and superconducting rock magnetometer used during Expedition 333.

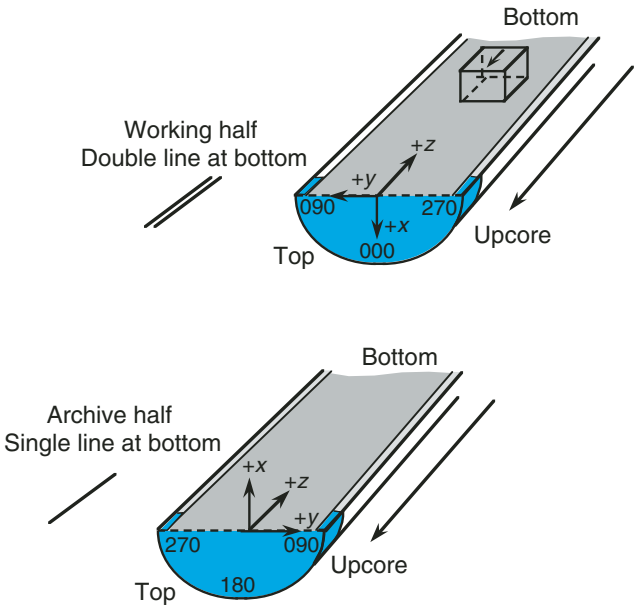

Figure F17. Example of visual core description (VCD) form used during Expedition 333.

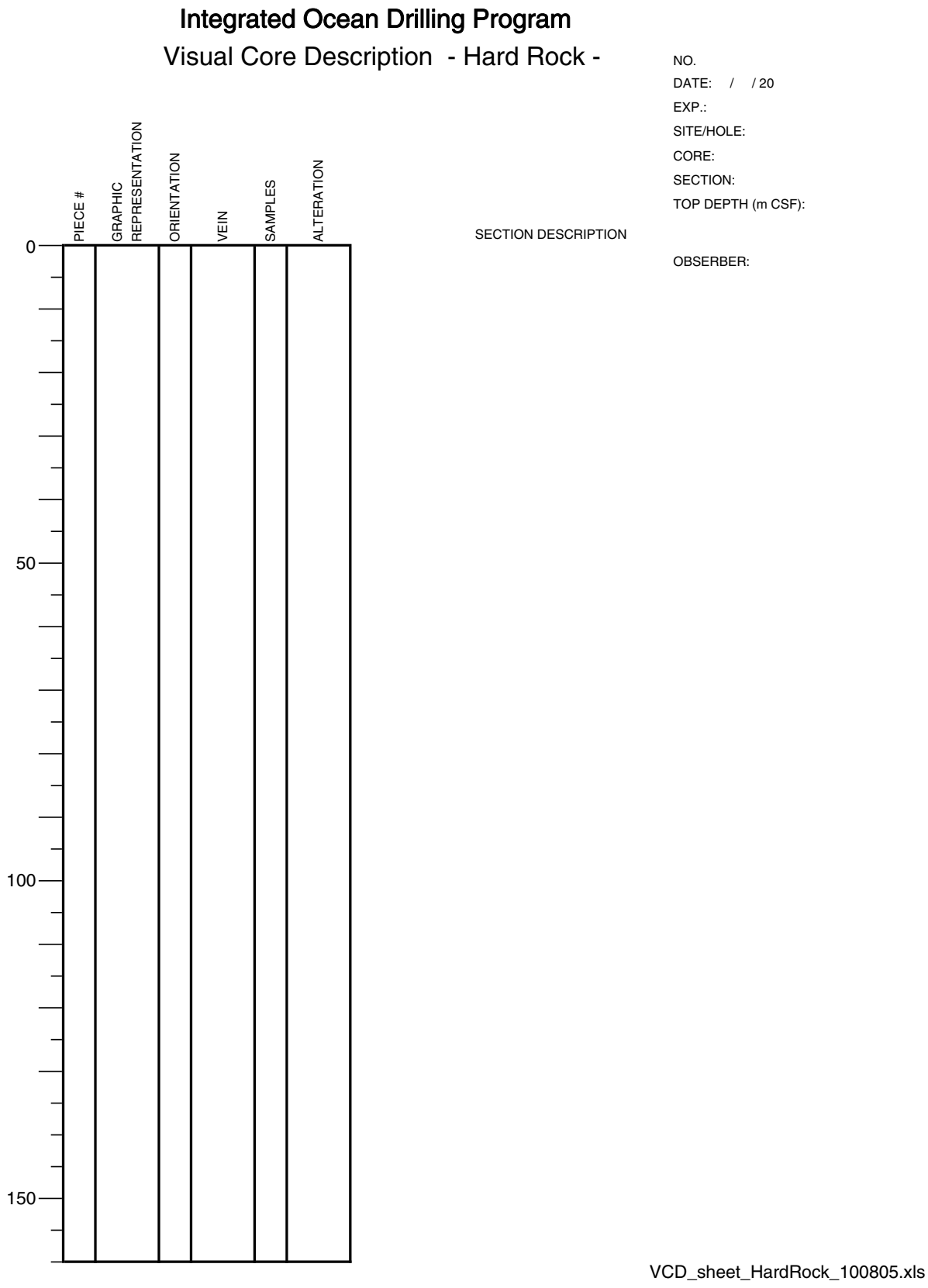

Figure F18. Graphic patterns for the lithologies and structural types encountered during Expedition 333.

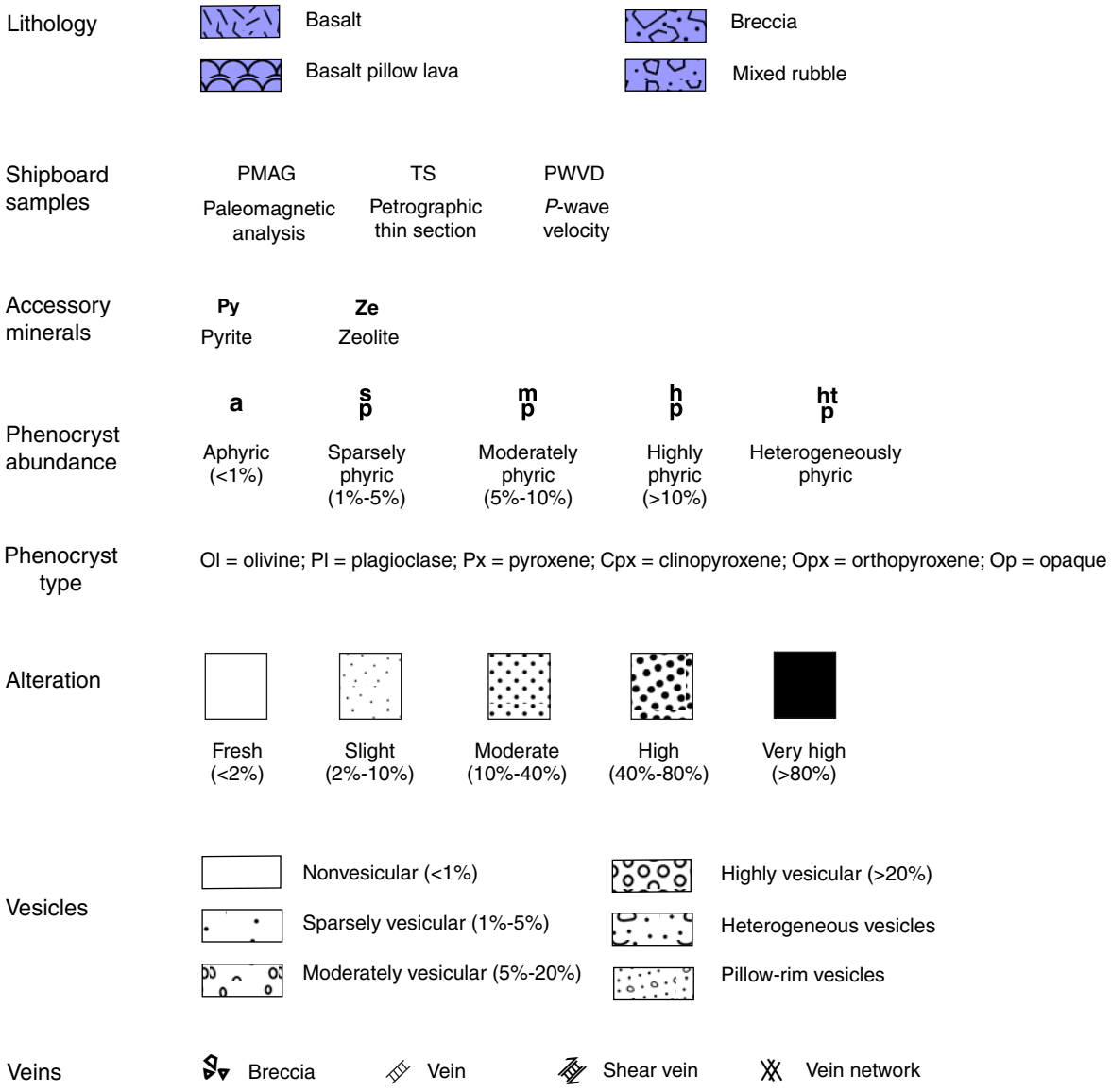

Table T1. Scan settings for X-ray CT scanner.

Parameter	Setting
Scan type	Helical-full-0.5 s
Interval (mm)	0.625
Gantry tilt	S0.0
SFOV	Small
Tube voltage (kV)	120
Tube current (mA)	100
Detector rows	16
Helical thickness (mm)	0.625
Pitch	0.562:1
Speed (mm/rot)	5.62
DFOV (cm)	9.6
R/L center (mm)	R0.0
A/P center (mm)	A0.0
Recon type	Detail
Matrix size (pixel)	512 × 512
Recon option	Full
Direct vis	Off

Protocol name: 090624_Exp319 9.1 071210_Aluminum Piece. SFOV = scan field of view, DFOV = dual field of view. R/L center = distance right or left of the center line, A/P center = distance anterior or posterior of the center line.

Table T2. Characteristic X-ray diffraction peaks for semiquantitative area analysis.

Mineral	Reflection	d-Value (Å)	Peak position (°2θ)
Composite clay	Multiple	4.478	19.4–20.4
Quartz	101	3.342	26.3–27.0
Plagioclase	002	3.192	27.4–28.2
Calcite	104	3.035	29.1–29.7

Table T3. Normalization factors for calculation of relative mineral abundance using bulk powder X-ray diffraction analysis.

Affected mineral in standard mixture:	Normalization factor			
	Total clay	Quartz	Plagioclase	Calcite
Influencing mineral:				
Total clay	9.8956702E–03	–1.5889532E–04	–2.8855808E–04	–7.3842803E–04
Quartz	–4.7221169E–05	5.8782392E–04	–4.7869325E–05	–3.1098843E–05
Plagioclase	7.2794763E–04	–4.2840613E–05	1.3719777E–03	–3.6005495E–05
Calcite	4.2042411E–05	3.3021188E–06	–4.1329499E–06	1.3071455E–03

Singular value decomposition was used to compute factors, following Fisher and Underwood (1995).

Table T4. Reference values of JB-1b reference material and daily measurements used for calibration of X-ray diffraction scanning data.

	JB-1b										
Major element oxide:	Na_2O_3	MgO	Al_2O_3	SiO_2	P_2O_5	K_2O	CaO	TiO_2	MnO	Fe_2O_3	Total
Reference value (wt%):	2.7	8.3	14.7	52.2	0.3	1.3	9.8	1.3	0.2	9.2	100
28 Dec 2010	ND	3.6	12.1	57.5	0.4	1.6	8.8	1.5	0.1	14.4	
29 Dec 2010	ND	3.6	12.5	57.0	0.5	1.5	9.0	1.5	0.1	14.4	
1 Jan 2011	1.0	3.6	11.8	51.4	0.6	2.1	12.1	1.9	0.0	15.6	
4 Jan 2011	0.8	4.1	11.7	51.3	0.6	2.1	12.3	1.8	0.1	15.2	
5 Jan 2011	4.3	4.6	8.1	47.2	0.7	2.2	13.1	2.0	0.1	17.8	
8 Jan 2011	1.0	6.1	15.4	53.6	0.5	1.7	9.6	1.4	0.1	10.6	
8 Jan 2011	1.1	6.4	15.3	53.3	0.4	1.7	9.7	1.4	0.1	10.5	

ND = Not determined.

Table T5. Astronomically calibrated age estimates of calcareous nannofossil datums used as biostratigraphic tie points, Expedition 333. (Continued on next page.)

Nannofossil event	Zone (base)	Degree of reliability	Age (Ma)
X medium *Gephyrocapsa* (>3.5 µm)–*Emiliania huxleyi*			0.082–0.063
FO *Emiliania huxleyi*	NN21	B	0.291
LO *Pseudoemiliania lacunosa*	NN20	A	0.436
LCO *Reticulofenestra asanoi*		A	0.905–0.901*
RE medium *Gephyrocapsa* (≥4 µm) + FO *Gephyrocapsa* sp. 3 (*G. parallela*)		A	1.04
FCO *Reticulofenestra asanoi*		D	1.136–1.078*
LO large *Gephyrocapsa* (>5.5 µm)		A	1.24
LO *Helicosphaera sellii*		C	1.34
FCO large *Gephyrocapsa* (>5.5 µm)			1.46
FO large *Gephyrocapsa* (>5.5 µm)		B	1.560–1.617*
LO *Calcidiscus macintyrei* (≥11 µm)		C	1.6
FO medium *Gephyrocapsa* (>3.5 µm)		A	1.67
LO *Discoaster brouweri*	NN19	A	2.06
AB *Discoaster triradiatus*		A	2.135–2.216*
LO *Discoaster pentaradiatus*	NN18	C	2.393–2.512*
LO *Discoaster surculus*	NN17	C	2.52
LO *Discoaster tamalis*		C	2.87
LO *Sphenolithus* spp.		C	3.65
LO *Reticulofenestra pseudoumbilicus* (>7 µm)	NN16	A	3.79
FCO *Discoaster asymmetricus*	NN15–NN14	B	4.13
LO *Amaurolithus primus*			4.5
LO *Ceratolithus acutus*		B	5.04
FO *Ceratolithus rugosus*	NN13	D	5.12
LO *Triquetrorhabdulus rugosus*			5.279*
FO *Ceratolithus acutus*		B	5.32
LO *Discoaster quinqueramus*	NN12	A	5.59
LO *Nicklithus amplificus*		A	5.978–5.939*
FO *Nicklithus amplificus*		C	6.909–6.684*
PE *Reticulofenestra pseudoumbilicus* (>7 µm)		D	7.077–7.167*
FO *Amaurolithus* spp./*Amaurolithus primus*	NN11b	A	7.362–7.424*
FCO *Discoaster surculus*		B	7.88
LCO *Minylitha convallis*		D	7.78–8.3
FO *Discoaster berggrenii*	NN11a	D	8.52
PB *Reticulofenestra pseudoumbilicus* (>7 µm)	NN10b	A	8.785–8.761*
FO *Discoaster pentaradiatus*			9.1
FO *Minylitha convallis*		D	9.416
LO *Discoaster hamatus*	NN10a	C	9.56
LO *Catinaster calyculus*		D	9.674*
LO *Catinaster coalitus*		D	9.687*
X *Discoaster hamatus–D. neohamatus*			9.762*
FO *Discoaster neohamatus*		C	9.867–10.521*
LCO *Discoaster exilis*			10.427
FO *Discoaster hamatus*	NN9	C	10.541
LO *Coccolithus miopelagicus*		C	10.613
FO *Discoaster calcaris*			10.676
FO *Discoaster bellus* gr.		C	10.72

Table T5 (continued).

Nannofossil event	Zone (base)	Degree of reliability	Age (Ma)
FO *Discoaster brouweri*		A	10.734–10.764*
FO *Catinaster calyculus*		D	10.785*
FO *Catinaster coalitus*	NN8	D	10.886–10.733*
LCO *Discoaster kugleri*		A	11.578–11.596*
FCO *Discoaster kugleri*	NN7	B	11.863–11.905*
LO *Cyclicargolithus floridanus*		D	12.037
LO *Coronocyclus nitescens*			12.254
LCO *Calcidiscus premacintyrei*		A	12.447
FCO *Triquetrorhabdulus rugosus*			12.671
LCO *Cyclicargolithus floridanus*		A	13.294
LO *Sphenolithus heteromorphus*	NN6	C	13.532–13.654*
LO *Helicosphaera ampliaperta*	NN5		14.914*
AE *Discoaster deflandrei*			15.663*
FO *Discoaster signus*			15.702*
FCO *Sphenolithus heteromorphus*			17.721*
LCO *Sphenolithus belemnos*	NN4		17.973*
LO *Triquetrorhabdulus carinatus*		D	18.315*
FO *Sphenolithus belemnos*	NN3		18.921*
FO *Helicosphaera ampliaperta*			20.393*
X *Helicosphaera euphratis–Helicosphaera carteri*			20.894*
FCO *Helicosphaera carteri*			21.985*
LCO *Triquetrorhabdulus carinatus*			22.092
FO *Sphenolithus disbelemnos*		C	22.413
FO *Discoaster druggii*	NN2	D	22.824*
LO *Sphenolithus delphix*		A	23.089
FO *Sphenolithus delphix*		A	23.356
LO *Sphenolithus ciperoensis*	NN1	C	24.389

Datums are based on Pacific records if not otherwise stated. * = datums based on Atlantic or Mediterranean records. Age estimates adopted from Raffi et al. (2006). X = abundance crossover, FO = first occurrence, LO = last occurrence, LCO = last consistent occurrence, RE = reentrance, FCO = first consistent occurrence, AB = acme beginning, AE = acme end, PE = paracme end, PB = paracme beginning. Degree of reliability: A = distinct, well defined, and isochronous worldwide; B = indistinct and less well defined but reasonably isochronous; C = distinct and well defined but diachronous; D = indistinct, poorly defined, and diachronous. See Raffi et al. (2006) for detailed explanation.

Table T6. Ages used for geomagnetic polarity timescale.

Age (Ma)		Chron/ subchron
Top	Bottom	
0	0.781	C1n
0.988	1.072	C1r.1n
1.173	1.185	C1r.2n
1.778	1.945	C2n
2.581	3.032	C2An.1n
3.116	3.207	C2An.2n
3.33	3.596	C2An.3n
4.187	4.3	C3n.1n
4.493	4.631	C3n.2n
4.799	4.896	C3n.3n
4.997	5.235	C3n.4n
6.033	6.252	C3An.1n
6.436	6.733	C3An.2n
7.14	7.212	C3Bn
7.251	7.285	C3Br.1n
7.454	7.489	C3Br.2n
7.528	7.642	C4n.1n
7.695	8.108	C4n.2n
8.254	8.3	C4r.1n
8.769	9.098	C4An
9.321	9.409	C4Ar.1n
9.656	9.717	C4Ar.2n
9.779	9.934	C5n.1n
9.987	11.04	C5n.2n
11.118	11.154	C5r.1n
11.554	11.614	C5r.2n
12.041	12.116	C5An.1n
12.207	12.415	C5An.2n
12.73	12.765	C5Ar.1n
12.82	12.878	C5Ar.2n
13.015	13.183	C5AAn
13.369	13.605	C5ABn
13.734	14.095	C5ACn
14.194	14.581	C5ADn
14.784	14.877	C5Bn.1n
15.032	15.16	C5Bn.2n
15.974	16.268	C5Cn.1n
16.303	16.472	C5Cn.2n
16.543	16.721	C5Cn.3n
17.235	17.533	C5Dn
18.056	18.524	C5En
18.748	19.722	C6n
20.04	20.213	C6An.1n
20.439	20.709	C6An.2n
21.083	21.159	C6AAn
21.659	21.688	C6AAr.2n
21.767	21.936	C6Bn.1n
21.992	22.268	C6Bn.2n
22.564	22.758	C6Cn.1n
22.902	23.03	C6Cn.2n

Data from Lourens et al. (2004).

Table T7. Shipboard and shore-based chemical analyses for samples collected during Expedition 333 including sample codes, sample volumes, and investigators.)

Sample code:	IWIC	IWICP	333HTIW	333MTIW1	333MTIW2	333MTIW3	333PHIW	333CDIW	Total volume
Investigator:	Shipboard	Shipboard	(Tomaru)	(Torres)	(Torres)	(Torres)	Henry	(Destrigneville)	
Type of analysis:	Alk, pH, Cl, IC	ICP-AES/MS, phosphate	δD, [I]	Sr isotopes	$\delta^{13}C$, DIC	REEs	Cl and O isotopes	Li isotopes	
Requested volume, container, and frequency:	4 mL Nalgene HDPE bottle, every IW	2 mL Nalgene HDPE bottle add 8 µL 6N HCl, every IW	1 mL Nalgene HDPE bottle, every IW	4 mL Nalgene HDPE bottle, every IW	2 mL septum screw-lid glass vials add 100 µL $HgCl_2$, every IW	7 mL Nalgene HDPE bottle, every IW	2 mL septum crimp-lid glass vials, 1/2 core	3 mL Nalgene HDPE bottle, 1/3 core	
Distributed volume - shallower (mL)	4	2	1	4	2	7	2	3	25
Distributed volume - deeper (mL)	1	2	1	4	2	7	2	3	22
Shore-based sample priority	—	—	4	1	3	6	2	5	

Names in parentheses are shore-based investigators. Alk = alkalinity, ICP-AES/MS = inductively coupled plasma–atomic emission spectrometry/mass spectrometry, DIC = dissolved inorganic carbon, REE = rare earth element, HDPE = high-density polyethylene, IW = interstitial water, — = not applicable.

Table T8. Expedition 333 interstitial water squeeze cake distribution for shore-based analyses.

Investigator	Sample code	Volume (cm^3)	Type of analyses	Comments
Archive	IWS	10.5–444.5		Store at 4°C
Destrigneville	333CDIWS	20	Li isotopes	Store at 4°C
Henry	333PHIWS	20	Cation exchange capacity	
Tomaru	333HTIWS	10	δD, [I]	Store at 4°C
Scudder	333RSIWS	20	Dispersed ash, geochemistry	